

# USING RANDOM SAMPLING CONSENSUS (RANSAC) TO DETECT ERRORS IN GLOBAL NAVIGATION SATELLITE SYSTEMS (GNSS) SIGNALS AND DATA

by

Nihar Shah, B.S., M.S.

December, 2021

Director of Thesis: Zhen Zhu, Ph.D.

Major Department: Mechanical Engineering

## **Abstract**

A positioning, navigation, and timing (PNT) signal can be used to estimate a user's position at an identified time. A global navigation satellite system (GNSS) uses the PNT signal to provide satellite-based navigation. Advanced receivers can track multiple GNSS constellations simultaneously. In order to have a robust and accurate solution, a user needs to detect any faulty measurements and data, and identify which satellite provided them so that faulty satellite can be excluded from a GNSS solution. Differencing techniques, such as time-differenced carrier phase (TDCP), provide for error reduction. The random sample consensus (RANSAC) method allows for the smoothing of data, even when there are a lot of gross errors present in the data set. The residuals from RANSAC and TDCP were studied to determine if they can be used to detect and identify error sources. A downsampling and thresholding method was able to identify first-order biases with slopes on the order of  $10^{-6}$  within minutes, while biases with slopes on the order of  $10^{-7}$  were identified on the order of one hour. The residuals from RANSAC and TDCP were ultimately able to detect and identify error sources.



# Using Random Sampling Consensus (RANSAC) to Detect Errors in Global Navigation Satellite Systems (GNSS) Signals and Data

A Thesis

Presented to the Faculty of the Department of Engineering  
East Carolina University®

In Partial Fulfillment of the Requirements for the Degree  
Masters of Science in Mechanical Engineering

by

Nihar Shah, B.S., M.S.

December, 2021

©2021, Nihar Shah

Using Random Sampling Consensus (RANSAC) to Detect Errors in Global Navigation  
Satellite Systems (GNSS) Signals and Data

by

Nihar Shah, B.S., M.S.

APPROVED BY:

Director of Thesis

---

Zhen Zhu, Ph.D.

Committee Member

---

Thad Wasklewicz, Ph.D.

Committee Member

---

Teresa Ryan, Ph.D.

Chair of the Department of Engineering

---

Barbara Muller-Borer, Ph.D.

Dean of the Graduate School

---

Paul J. Gemperline, Ph.D.

# Contents

<b>List of Tables</b>	<b>v</b>
<b>List of Figures</b>	<b>vi</b>
<b>List of Acronyms</b>	<b>viii</b>
<b>1 Introduction</b>	<b>1</b>
<b>2 Literature Review</b>	<b>5</b>
2.1 The Measurement Equation . . . . .	5
2.2 Sources of Error . . . . .	6
2.3 Error Reduction and Time-Differenced Carrier Phase . . . . .	8
2.4 Trajectory Correction . . . . .	9
2.5 Random Sampling Consensus . . . . .	10
2.6 Time-Variant Stochastic Statistics . . . . .	11
<b>3 Methodology</b>	<b>14</b>
3.1 Corrected TDCP Measurements . . . . .	14
3.2 Correction Terms . . . . .	16
3.3 Impact of Satellite Clock and Orbit Errors . . . . .	16
3.4 Using RANSAC with Instantaneous Measurements . . . . .	17
3.5 Simulated Bias in Satellite Orbit . . . . .	18
3.6 Downsampling and Thresholding . . . . .	19
<b>4 Results and Analysis</b>	<b>21</b>
4.1 SP3 Corrections . . . . .	21
4.2 Autocorrelation . . . . .	23
4.3 Allan Variance . . . . .	26
4.4 Elevation Angle . . . . .	28
4.5 Autocorrelation of Truncated Data . . . . .	32
4.6 Allan Variance Analysis of Truncated Data . . . . .	34
4.7 Downsampling and Thresholding . . . . .	37
4.8 Simulated Bias in Satellite Orbit . . . . .	45

<b>5 Conclusion</b>	<b>53</b>
5.1 Detect and Identify Error Sources . . . . .	53
5.2 Recommendations for Future Work . . . . .	54
<b>References</b>	<b>56</b>

# List of Tables

2.1	Definition of terms in Equation 2.1 . . . . .	5
2.2	Expected log-log slopes of Allan variance for common noise types . . . . .	12
3.1	Definition of terms in Equation 3.1 . . . . .	15
3.2	Definition of terms in Equation 2.1 to account for TDCP . . . . .	15
4.1	Summary statistics of differences between original and Standard Product #3 (SP3)-corrected residuals . . . . .	23
4.2	Time (in $s$ ) to identify simulated bias of $1 \times 10^{-4}$ . . . . .	48
4.3	Time (in $s$ ) to identify simulated bias of $5 \times 10^{-5}$ . . . . .	48
4.4	Time (in $s$ ) to identify simulated bias of $1 \times 10^{-5}$ . . . . .	48
4.5	Time (in $s$ ) to identify simulated bias of $5 \times 10^{-6}$ . . . . .	49
4.6	Time (in $s$ ) to identify simulated bias of $1 \times 10^{-6}$ . . . . .	49
4.7	Time (in $s$ ) to identify simulated bias of $5 \times 10^{-7}$ . . . . .	49
4.8	Time (in $s$ ) to identify simulated bias of $1 \times 10^{-7}$ . . . . .	49

# List of Figures

1.1	Finding two positions $O$ in two-dimensional space using range from two satellites	3
2.1	Faulty orbital model leading to orbital error	7
2.2	Antenna receiving a direct path signal and a reflected path signal, leading to multipath error	8
3.1	Overview of satellite and receiver motion	14
4.1	Comparison of original and SP3-corrected residuals for satellite 14	22
4.2	Comparison of original and SP3-corrected residuals for satellite 31	22
4.3	Normalized autocorrelation for satellite 14	23
4.4	Normalized autocorrelation for satellite 14 with primary peak highlighted	24
4.5	Normalized autocorrelation for satellite 31	25
4.6	Normalized autocorrelation for satellite 31 with primary (red) and secondary (blue) peaks highlighted	25
4.7	Allan variance analysis for satellite 14	27
4.8	Allan variance analysis for satellite 31	28
4.9	Elevation angle of satellite 14	28
4.10	Corrected residuals from satellite 14, channel 1 with a 250-point centered moving average	29
4.11	Corrected residuals from satellite 14, channel 1 with a 250-point centered moving average and approximation of the moving average	29
4.12	Elevation angle of satellite 31	30
4.13	Corrected residuals from satellite 31, channel 1 with a 250-point centered moving average	31
4.14	Corrected residuals from satellite 31, channel 1 with a 250-point centered moving average and approximation of the moving average	31
4.15	Normalized autocorrelation for truncated satellite 14 residuals	32
4.16	Comparison of original residuals and truncated residuals for satellite 14	33
4.17	Normalized autocorrelation for truncated satellite 31 residuals	33
4.18	Comparison of original residuals and truncated residuals for satellite 31	34
4.19	Allan variance analysis for truncated residuals from satellite 14	35
4.20	Allan variance analysis for truncated residuals from satellite 31	36
4.21	Variation of initialization and window sizes for satellite 14, Part A	38

4.22	Variation of initialization and window sizes for satellite 14, Part B . . . . .	39
4.23	Percentage of points identified as outliers versus initialization period . . . . .	40
4.24	Percentage of points identified as outliers versus window size . . . . .	40
4.25	Variation of initialization and window sizes for satellite 31, Part A . . . . .	42
4.26	Variation of initialization and window sizes for satellite 31, Part B . . . . .	43
4.27	Percentage of points identified as outliers versus initialization period . . . . .	44
4.28	Percentage of points identified as outliers versus window size . . . . .	44
4.29	Variation of added bias, initialization period, and window size for residuals for satellite 14, Part A . . . . .	46
4.30	Variation of added bias, initialization period, and window size for residuals for satellite 14, Part B . . . . .	47
4.31	Variation of added bias, initialization period, and window size for residuals for satellite 31, Part A . . . . .	51
4.32	Variation of added bias, initialization period, and window size for residuals for satellite 31, Part B . . . . .	52

# List of Acronyms

<b>ADR</b>	accumulated Doppler range
<b>AOA</b>	angle of arrival
<b>BDS</b>	BeiDou Navigation Satellite System
<b>CA</b>	coarse/acquisition
<b>CDDIS</b>	Crustal Dynamics Data Information System
<b>CEI</b>	clock, ephemeris, integrity
<b>CL</b>	civil-long
<b>CM</b>	civil-moderate
<b>GLONASS</b>	Global'naya Navigatsionnaya Sputnikovaya Sistema
<b>GNSS</b>	global navigation satellite system
<b>GPS</b>	Global Positioning System
<b>IGS</b>	International Global Navigation Satellite System Service
<b>INU</b>	inertial navigation unit
<b>IRNSS</b>	Indian Regional Navigation Satellite System
<b>k-NN</b>	$k$ -nearest-neighbor
<b>NASA</b>	National Aeronautics and Space Administration
<b>NavIC</b>	Navigation with Indian Constellation

<b>P</b>	precision
<b>PNT</b>	positioning, navigation, and timing
<b>PRN</b>	pseudorandom noise
<b>QZSS</b>	Quasi-Zenith Satellite System
<b>RANSAC</b>	random sample consensus
<b>RMS</b>	root-mean-square
<b>RSS</b>	relative signal strength
<b>RTK</b>	real-time kinematic
<b>SP3</b>	Standard Product #3
<b>SPP</b>	single point positioning
<b>SWaP</b>	size, weight, and power
<b>TDCP</b>	time-differenced carrier phase
<b>TDOA</b>	time difference of arrival
<b>TOA</b>	time of arrival
<b>TOF</b>	time of flight

# Chapter 1

## Introduction

A positioning, navigation, and timing (PNT) radio signal can be used to estimate a user's navigation solution. A PNT receiver processes the transmitter's signal to extract ranging measurements and other parameters of interest, which are used to compute a user's position and/or clock solution.<sup>29</sup>

The general term for satellite-based navigation systems is global navigation satellite system (GNSS). In the United States, our primary GNSS is Global Positioning System (GPS). It was designed for PNT of aircraft and other types of vehicles. Additionally, GPS is critical in less-obvious uses, such as banking, telecommunications, weather, seismology, power synchronization, and atmospheric research.<sup>23</sup> The need for accurate civilian GPS service was addressed by President Clinton as early as 2000.<sup>10</sup> The problems with GPS accuracy, availability, integrity, and reliability were identified at the Presidential level as early as 2004.<sup>7</sup> The impacts of degraded GPS continue to affect all levels of national security, as identified in multiple national strategy documents that are applicable at the time this thesis was authored.<sup>43,45,46</sup> Other GNSS systems around the world include:<sup>24</sup>

- BeiDou Navigation Satellite System (BDS), owned by China
- Galileo, owned by the European Union

- Global'naya Navigatsionnaya Sputnikovaya Sistema (GLONASS), owned by the Russian Federation

The Indian Regional Navigation Satellite System (IRNSS)/Navigation with Indian Constellation (NavIC) (owned by the Government of India) and Quasi-Zenith Satellite System (QZSS) (owned by the Government of Japan) operate regionally over India and Japan, respectively, but not globally.<sup>24</sup>

As of 2019, there were over 120 GNSS satellites worldwide.<sup>51</sup> The United States' GPS transmits signals at two frequencies ( $L1 = 1575.42 \text{ MHz}$  and  $L2 = 1227.6 \text{ MHz}$ , or 154 and 120 times the internal clock frequency of  $10.23 \text{ MHz}$ , respectively).<sup>32,33,44,52</sup> Each signal is encoded by mod-2 addition (can also be considered to be a logical “exclusive or” or XOR) of a pseudorandom noise (PRN) ranging code and navigation data.<sup>33</sup> The  $L1$  signal has two codes in quadrature: a coarse/acquisition (CA) and a precision (P) code.<sup>32</sup> The  $P$ -code also has an anti-spoofing mode that is reserved for military use.<sup>32</sup> The  $L2$  signal provides a more accurate timing signal using the  $L2$  civil-moderate (CM) and  $L2$  civil-long (CL) codes.<sup>32</sup> The  $L5$  signal is the newest signal that has a faster acquisition time and provides increased accuracy by implementing a new ranging signal, synchronization, and civil navigation data.<sup>33</sup>

To acquire signals from the satellites, receivers use the predicted position calculated with navigation data.<sup>29</sup> Receivers use a locally-generated copy of the code to determine the time of reception. Based on the fact that the signal travels at a known speed (the speed of light), receivers are able to calculate the distance between the transmitter and receiver.<sup>29</sup> Two satellites ( $S_1$  and  $S_2$ ) can be used to calculate user position ( $U$ ) in the two-dimensional case, as illustrated in Figure 1.1.<sup>57</sup>

There are two possible points that result from the calculation with  $S_1$  and  $S_2$ ; the closer of the two points is defaulted to being the correct point.<sup>29</sup> A third satellite is needed to calculate user position in the three-dimensional case.<sup>29</sup> All of the calculations assume that the clocks on the transmitter and receiver are perfectly synchronized; a fourth satellite is

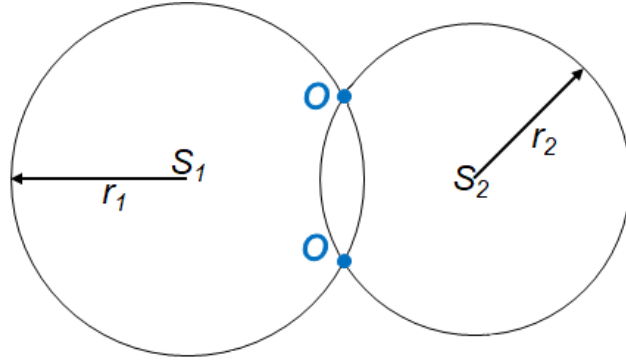


Figure 1.1: Finding two positions  $O$  in two-dimensional space using range from two satellites

needed to resolve the difference in satellite and user timing in the three-dimensional case.<sup>29,57</sup> At any given time, a user in the United States can expect to have six to eight GPS satellites within line of sight.<sup>16</sup>

Advanced receivers can track multiple GNSS constellations simultaneously.<sup>66</sup> All of these signals can be integrated to increase the accuracy and reliability of PNT with a minimal increase in size, weight, and power (SWaP); and cost.<sup>66</sup> Since more GNSS constellations can be observed, there is greater redundancy in satellite signals. Integrating and comparing data from different GNSS allows for the identification of errors.<sup>11</sup>

In order to have a robust and accurate solution, a user needs to detect and identify any faulty measurements and data, so that faulty satellite(s) can be excluded from a GNSS solution.<sup>66</sup> For example, multipath is considered an error source for GNSS ranging measurement. However, if a reflected signal is received instead of the direct line of sight signal, it is considered a faulty measurement. Another example is error in satellite clock and orbit models: if the broadcast satellite model has an error that drifts beyond acceptable tolerance, the satellite must be identified and detected. Satellite faults can be observed in measurement residuals.<sup>11,60,66</sup>

Some error sources can be reduced via differencing. For example, time-differenced carrier phase (TDCP) can reduce some of the biases in the solution calculations by differencing

successive carrier phase measurements.<sup>66</sup> Additionally, methods such as random sample consensus (RANSAC) can be used with multi-GNSS receivers to detect and remove bias in TDCP measurements.<sup>66</sup> The two research questions for this thesis are:

1. Can residuals from RANSAC and TDCP be used to detect and identify error sources?
2. If so, what types of errors can it detect?

Chapter 2 will review the literature and concepts used for this research. Chapter 3 will summarize the analysis methodology. Chapter 4 will summarize the analysis results. Finally, Chapter 5 will summarize the conclusions and recommendations.

# Chapter 2

## Literature Review

### 2.1 The Measurement Equation

The general measurement equation of a GNSS navigation system is given by Equation 2.1.<sup>67</sup> The terms in Equation 2.1 are defined in Table 2.1.<sup>67</sup>

$$\mathbf{z} = \mathbf{H}\mathbf{x} + \boldsymbol{\epsilon} + \mathbf{f} \quad (2.1)$$

Term	Definition
$\mathbf{z}$	Observed position measurements
$\mathbf{H}$	Geometric matrix
$\mathbf{x}$	True state
$\boldsymbol{\epsilon}$	Nominal errors
$\mathbf{f}$	Faults

Table 2.1: Definition of terms in Equation 2.1

The nominal errors  $\boldsymbol{\epsilon}$  are errors that can be modeled. The faults  $\mathbf{f}$  include biases in  $\mathbf{z}$  and/or  $\mathbf{H}$ , that are not captured by  $\boldsymbol{\epsilon}$ .

## 2.2 Sources of Error

Previous work has identified six nominal sources of GPS carrier phase error  $\epsilon$  in calculating user position:<sup>50,56,67</sup>

1. Ionospheric delay
2. Tropospheric delay
3. Noise
4. Satellite orbit prediction
5. Inter-system bias
6. Signal multipath

Significant variations in electron density in the ionosphere result in a contribution to ranging errors.<sup>61</sup> Delays in ranging code and change of carrier phase lead to ranging errors, which can aggregate as trends.<sup>29</sup> The ionospheric delay is frequency-dependent, so a dual-frequency receiver can be used to cancel out this error; however, the process magnifies any other measurement errors present in the solution.<sup>29</sup> If using a single-frequency measurement, the ionospheric delay may contribute anywhere from 9.8 *m* to 19.6 *m* to the overall error.<sup>44</sup> Similarly, tropospheric delay can increase ranging errors up to 2.4 *m* if they are not corrected with a model.<sup>29,38,58</sup> Ionospheric models are able to correct about 50% to 70% of the ionospheric error, while tropospheric models can correct over 90% of the tropospheric error.<sup>29</sup> Both types of atmospheric effects can be modeled as biases or first-order deviations in TDCP.<sup>34</sup>

Different sources of noise caused by other gradients can further contribute to error.<sup>66</sup> Thermal noise is the dominant source of noise, and is evaluated with the carrier-to-noise ratio ( $C/N_0$ ).<sup>29</sup> The  $C/N_0$  is affected by the elevation angle between the satellite and the user, since the signal interacts with more of the atmosphere at low elevation angles of 15° or lower.<sup>29</sup> The low elevation angle can lead to error contributions on the order of 10 *m*.<sup>29</sup> Physical

environmental factors (*e.g.*, thermal noise) can be modeled as a random walk process, while non-stationary noise can be modeled as Gauss-Markov processes.<sup>62,68</sup>

Errors in satellite orbit prediction (caused by inconsistent data, spoofing, drifts, etc.) can result in large biases in the user positioning solution, as illustrated in Figure 2.1. Between 2008 and 2014, the average nominal error in orbit prediction for GPS satellites was 52 *cm*.<sup>29</sup> Faults in satellite clock or orbit can be significantly greater. For example, on April 1, 2014, GLONASS satellites transmitted incorrect broadcast messages that resulted in errors on the order of 200 *km*.<sup>3</sup> The erroneous positioning data was likely caused by a “bad” software update.<sup>3</sup> A sudden change in the prediction model would appear as a bias or first-order deviation in TDCP.<sup>34</sup>

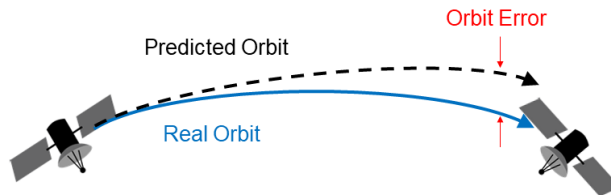


Figure 2.1: Faulty orbital model leading to orbital error

Inter-system bias is caused by timing differences between different GNSS constellations.<sup>56</sup> Differencing methods can be used to reduce this error, and are further described in Section 2.3.

The broadcast signal from the GPS satellites can be reflected or diffracted just like any other type of electromagnetic wave, leading to a GNSS ranging error source known as multipath.<sup>31</sup> Multipath is illustrated in Figure 2.2.<sup>54</sup> Since the reflected signal (red dashed line in Figure 2.2) takes longer to reach the antenna, the range calculation produces an erroneous value (blue dot at the end of the dotted line in Figure 2.2).<sup>31</sup> Statistically, multipath errors can be modeled as a Gauss-Markov stochastic process.<sup>30</sup> Further, the multipath error model used by an autonomous vehicle in a city will be different than that of a commercial airliner flying over an ocean. Since multipath error is so highly dependent on the environment, there

are not unified models to mitigate it like there are for tropospheric delay.<sup>31</sup>

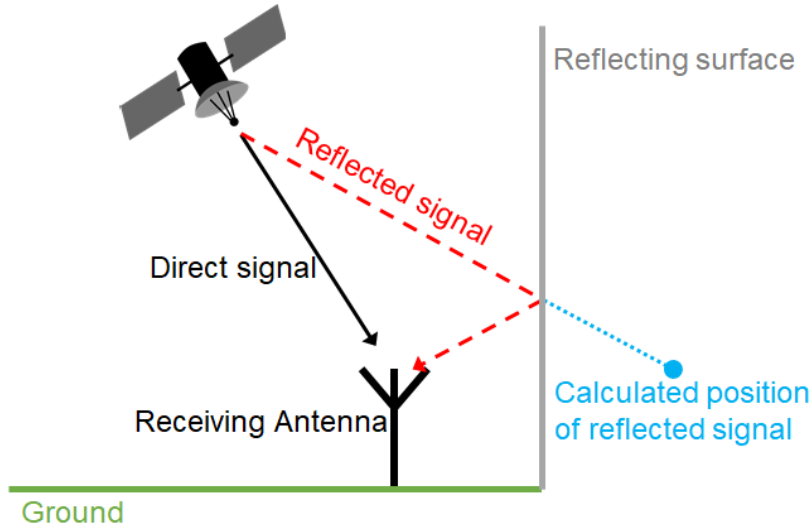


Figure 2.2: Antenna receiving a direct path signal and a reflected path signal, leading to multipath error

## 2.3 Error Reduction and Time-Differenced Carrier Phase

Differencing techniques provide for error reduction. Single differencing the carrier phase signal compares the received signal from one satellite to two antennas.<sup>20</sup> Single differencing cancels out the common effects shared by signals from a satellite taking different paths, such as atmospheric effects like ionospheric delay and tropospheric delay.<sup>20</sup> In double differencing, two single-differenced signals are subtracted from each other.<sup>1,59</sup> Double-differencing reduces errors in satellite orbit prediction, clock drift, and receiver clock bias.<sup>20</sup>

Using the PRN code to determine user position is a single point positioning (SPP) solution, which provides positioning accuracy on the order of a few meters.<sup>5,29</sup> Incorporating the carrier-phase observations can allow for a position accuracy on the order of centimeters or less; however, the carrier-phase measurement is ambiguous because the number of integer multiples of a complete cycle is unknown.<sup>5</sup> One of the ambiguity resolution techniques

is real-time kinematic (RTK), which uses some type of base station from which the measurements are differenced against those from the user.<sup>29</sup> The RTK method does not require hours for the correct solution to converge, but it does require precise estimates of the initial carrier-phase ambiguity to work effectively.<sup>5</sup>

Alternatively, instead of differencing a signal received by two antennas, successive carrier phase measurements are differenced in the time-differenced carrier phase (TDCP) method.<sup>59,66</sup> With TDCP, range change can be measured by differencing accumulated Doppler range (ADR) over time. Using pseudorange instead of ADR leads to a more noisy result by a factor of about 10.<sup>64</sup> With the TDCP method, inter-constellation timing bias and several other error sources are canceled out, allowing one measurement equation to be used for all satellites and constellations.<sup>66</sup> With more available satellites, the solution would offer high reliability in near real-time, but would have a higher computational cost.<sup>66</sup>

Using TDCP brings about two new problems. First, there are more data sources to filter through to find faulty signals. Second, since several biases are differenced out, biases that remain close to constant over time may be obfuscated.

## 2.4 Trajectory Correction

The accuracy of the SPP or TDCP solution is directly related to the accuracy of the GNSS orbit and clock information used to calculate the solution.<sup>40</sup> Models of a satellite's motion can be used to compute a reference trajectory which includes satellite ephemeris and clock estimates.<sup>29</sup> A least-squares-fit routine converts the predicted positions (based on the reference trajectory and the position estimates) into positioning solutions.<sup>32</sup>

Each of the GPS satellites provides a unique clock, ephemeris, integrity (CEI) data that is needed to provide a positioning solution.<sup>32,33</sup> The CEI data includes information such as satellite-specific clock correction polynomial parameters, ephemeris parameters, and health

flags.<sup>32,33</sup> These calculations are typically accurate from 5 *m* to 10 *m*.<sup>28</sup>

The International Global Navigation Satellite System Service (IGS) calculates high-accuracy satellite orbit solutions and provides them to National Aeronautics and Space Administration (NASA) Crustal Dynamics Data Information System (CDDIS) for archival in a format called Standard Product #3 (SP3).<sup>40</sup> The SP3 format provides satellite orbit data that is either measured from the broadcast signal, based on an interpolation, or extrapolated (or predicted) from an orbit model.<sup>27</sup> The IGS orbits are calculated using a weighted linear combination of solutions from up to eight separate analysis centers.<sup>2,26</sup> First, differences in reference frames are removed from each center’s solution.<sup>2</sup> Then, a seven-parameter Helmert transformation is estimated for each solution to further reduce errors caused by reference frame misalignment.<sup>2</sup>

The IGS has three forms of the data: ultra-rapid, rapid, and final.<sup>40</sup> The ultra-rapid data are comprised of fits to observational data for the first half and predicted orbits for the second half.<sup>26</sup> The rapid data are daily solutions that are released approximately 17 *hrs* after the end of each day.<sup>40</sup> The final data are the most accurate solutions and are weekly solutions released approximately 13 days after the end of each week.<sup>40</sup>

A user can use a simple GNSS receiver to collect pseudorange and carrier phase and post-process the received measurements with corrected satellite position and clock data to produce a more accurate solution.<sup>48</sup> The SP3-corrected data has positional accuracies on the order of 20 *mm*,<sup>26</sup> which is 500 times more accurate than the accuracy of the CEI data alone. Therefore, the SP3-corrected data can be used as truth data for comparative analyses.

## 2.5 Random Sampling Consensus

Traditional methods for fitting models to data (such as the method of least squares) assume that there are enough “good” values to smooth out any large deviations.<sup>17</sup> However,

this is not always true for some applications, include GNSS. The RANSAC method allows for finding an error-free subset, even when there are multiple gross errors present in the data set.<sup>17</sup> The general RANSAC method helps identify the inliers  $\theta$  from a set of  $N$  observations to solve for state vector  $x$ , even if there are multiple simultaneous outliers.<sup>67</sup>

The process was initially developed for image analysis and automated cartography, but was then applied to generalized model fitting to estimate unknown parameters in data with numerous outliers to improve fault detection.<sup>17,66</sup> The application of RANSAC methods has been demonstrated in single GNSS constellations,<sup>8,49</sup> but due to the limited number of satellites, there is minimal benefit from applying RANSAC.<sup>66</sup> In a multi-GNSS problem, the use of RANSAC would have a more significant impact.<sup>66</sup> RANSAC can also be used to identify faulty measurements in GNSS.

## 2.6 Time-Variant Stochastic Statistics

Each GNSS satellite suffers from errors such as multipath, receiver noise, interference, troposphere error, and ionosphere gradients.<sup>14</sup> While TDCP can minimize these errors, there will be some residuals from each signal.<sup>56</sup>

The root-mean-square (RMS) residuals between each individual satellite's TDCP and calculated truth reference value can be analyzed to identify different types of trends.<sup>56,66</sup> There are five main random processes commonly related to GNSS data: Quantization noise, White noise, Flicker noise, Random walk, and Gauss-Markov process.<sup>15,41</sup> Quantization noise comes from analog to digital conversions.<sup>25</sup> Random white noise will have very low autocorrelation, and can often be modeled using Gaussian distributions with a long-term average of zero.<sup>35,47,63</sup> Flicker noise is a measure of the bias offset.<sup>35,47</sup> The random walk errors are “a random process of uncertain origin, possibly known as a very low-frequency noise term”<sup>47</sup> possibly caused by tropospheric delays.<sup>35</sup> Gauss-Markov processes are processes that are

Table 2.2: Expected log-log slopes of Allan variance for common noise types

Noise type	Curve Slope
Quantization noise	-1
White noise	-1/2
Flicker noise	0
Random walk	+1/2
Gauss-Markov process	-1/2 then + 1/2

exponentially autocorrelated with time.<sup>47</sup>

A commonly accepted method for studying the residuals is by using Allan variance.<sup>41,47</sup> The Allan variance method was initially used to study frequency stability in clocks and electronics, but was later applied to navigation systems to identify processes in random drift errors over time, to characterize inertial errors, and to identify stochastic processes.<sup>41,42,65</sup> One advantage of the Allan variance is that it converges for most types of clock noise based on the resulting slope, as summarized in Table 2.2.<sup>19,36,41,50</sup> Additionally, it identifies the impact of stochastic processes when using different time periods to average the data.<sup>19</sup> Time periods where the Allan variance is low identify averaging periods where the impacts of stochastic processes are minimized.<sup>19</sup>

Kalman filters are often applied to GNSS data to combine different data sources; however, the Kalman filter requires the inputs to be white noise.<sup>41</sup> Instead of assuming that the data is white noise (or approximates white noise), the Allan variance analysis can be used to verify the validity of the white noise assumption.<sup>41</sup> If there are other stochastic processes present besides white noise, the Allan variance analysis would be able to identify them and allow the user to compensate the model accordingly.<sup>41</sup>

The work in this thesis attempts to identify zeroth- and first-order biases (points and linear biases), not traditional GNSS anomalies and faults. There are several methods that can be used to detect these biases. There are three general categories of detection methods: supervised, semi-supervised, and unsupervised.<sup>22</sup> Supervised methods require a labeled

set of training data of “good” and “bad” data.<sup>9</sup> Semi-supervised methods have labels for only “good” data.<sup>9</sup> Unsupervised methods do not require training data, and are the most applicable to this research.<sup>9</sup>

A simple global bias detection method identifies the distance a point is from the  $k$  nearest neighboring data points, and is appropriately named  $k$ -nearest-neighbor (k-NN) method.<sup>22</sup> The value of  $k$  used directly affects the effectiveness of the k-NN method. If  $k$  is too low, there are not enough data points to produce a reliable calculation; if  $k$  is too large, the estimate may be too coarse.<sup>22</sup> Typically,  $k$  is in the range  $10 < k < 50$ .<sup>22</sup> For GNSS bias detection, the balance of low and high  $k$  values is a balance of effectiveness and timeliness.

# Chapter 3

## Methodology

### 3.1 Corrected TDCP Measurements

As illustrated in Figure 3.1, the  $j^{\text{th}}$  satellite in the  $k^{\text{th}}$  constellation moves over a time period from position  $\mathbf{S}(t_0)$  to  $\mathbf{S}(t_1)$ . The  $i^{\text{th}}$  ground antenna/receiver moves from position  $\mathbf{U}(t_0)$  to  $\mathbf{U}(t_1)$ . The unit vector  $\mathbf{e}_i^j$  identifies the direction from the ground receiver to the satellite, while  $\mathbf{R}_i^j$  gives the distance.

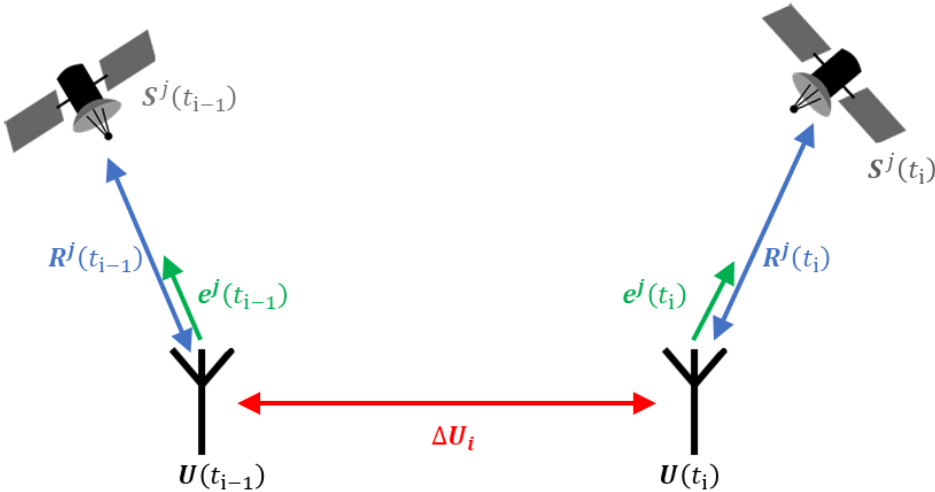


Figure 3.1: Overview of satellite and receiver motion

The corrected TDCP measurements from the  $i^{\text{th}}$  antenna/receiver to the  $l^{\text{th}}$  channel

on the  $j^{\text{th}}$  satellite in the  $k^{\text{th}}$  constellation is described in Equation 3.1.<sup>50,66</sup> The terms in Equation 3.1 are defined in Table 3.1.<sup>50,66</sup>

$$ADR_i^{j,k,l}(t_1) - ADR_i^{j,k,l}(t_0) - corr_{SV} - corr_{geo} = -\mathbf{e}_i^j(t_1)\Delta\mathbf{U} + \Delta b_i + \Delta f_i^{j,k,l} + \epsilon_i^{j,k,l}(t) \quad (3.1)$$

<b>Term</b>	<b>Definition</b>
$ADR$	ADR
$corr_{SV}$	Satellite Doppler correction term
$corr_{geo}$	Geometric correction term
$\mathbf{e}_i^j$	Unit vector from the $i^{\text{th}}$ antenna/receiver $U$ to the $j^{\text{th}}$ satellite $S$
$\Delta\mathbf{U}$	Displacement of the receiver from time $t_0$ to $t_1$
$\Delta b_i$	Receiver clock bias
$\Delta f_i^{j,k,l}$	Contribution of faults on the ADR measurement
$\epsilon_i^{j,k,l}$	Noise and all remaining residual errors after time differencing

Table 3.1: Definition of terms in Equation 3.1

The residual errors  $\epsilon_i^{j,k,l}$  are comprised of time-variant sources such as troposphere residuals  $\Delta T_i^j$ , ionosphere residuals  $\Delta I_i^{j,l}$ , inter-system bias  $\Delta\beta^{j,k,l}$ , multipath errors  $\Delta M_i^{j,k,l}$ , and noise  $\Delta\epsilon_i^{j,k,l}$ .<sup>50</sup> These individual components to the overall residual errors can be assumed to be rapidly changing, but with a combined magnitude of error on the order of millimeters per second with a one-second differencing.<sup>50</sup>

The measurement equation described in Equation 2.1 can be reused to account for the TDCP methodology. Table 2.1 would be redefined to Table 3.2.

<b>Term</b>	<b>Definition</b>
$\mathbf{z}$	ADR
$\mathbf{H}$	Geometric matrix
$\mathbf{x}$	TDCP measurements
$\boldsymbol{\epsilon}$	Nominal errors
$\mathbf{f}$	Faults

Table 3.2: Definition of terms in Equation 2.1 to account for TDCP

## 3.2 Correction Terms

The TDCP reflects changes in distances in line of sight. It needs to be corrected with satellite motion and geometric change between the satellite and user motion directly. The satellite correction term and the geometric correction term are given by Equation 3.2 and Equation 3.3, respectively.<sup>59</sup>

$$corr_{SV} = \mathbf{S}^j(t_1) \cdot \mathbf{e}_i^j(t_1) - \mathbf{S}^j(t_0) \cdot \mathbf{e}_i^j(t_0) \quad (3.2)$$

$$corr_{geo} = \mathbf{U}_i(t_1) \cdot \mathbf{e}_i^j(t_1) - \mathbf{U}_i(t_0) \cdot \mathbf{e}_i^j(t_0) \quad (3.3)$$

The generalized unit vector  $\mathbf{e}_i^j(t)$  is defined in Equation 3.4.<sup>59</sup>

$$\mathbf{e}_i^j(t) = \frac{\mathbf{S}^j(t) - \mathbf{U}_i(t)}{|\mathbf{S}^j(t) - \mathbf{U}_i(t)|} \quad (3.4)$$

## 3.3 Impact of Satellite Clock and Orbit Errors

The distance between the satellite and the antenna/receiver is typically ranges from 6400 *km* to 67,000 *km*,<sup>32</sup> so the impact of a small satellite position error on  $\mathbf{e}_i^j(t)$  will be negligible. Therefore, Equation 3.2 can be rewritten as Equation 3.5. In Equation 3.5,  $\Delta \mathbf{S}_b^j(t) \cdot \mathbf{e}_i^j(t)$  represents the satellite position error projected onto the unit vector at the identified time.

$$\Delta corr_{SV} = \Delta \mathbf{S}_b^j(t_1) \cdot \mathbf{e}_i^j(t_1) - \Delta \mathbf{S}_b^j(t_0) \cdot \mathbf{e}_i^j(t_0) \quad (3.5)$$

If the satellite clock or orbit model are erroneous, there will also be an additional time-differenced satellite clock error of  $\Delta \beta_b^{j,k,l}$ . This would yield the satellite fault model in Equation 3.6.

$$\Delta f_{i,SV}^{j,k,l} = \Delta \beta_b^{j,k,l} + (\Delta \mathbf{S}_b^j(t_1) \cdot \mathbf{e}_i^j(t_1) - \Delta \mathbf{S}_b^j(t_0) \cdot \mathbf{e}_i^j(t_0)) \quad (3.6)$$

The term  $\Delta f_{i,SV}^{j,k,l}$  is a component of  $\Delta f_i^{j,k,l}$  from Equation 3.1. The error calculated by  $\epsilon_i^{j,k,l}(t)$  is the error in satellite based on truth data. If real-time data is aggregated, there is no direct estimate of truth  $\Delta U$ . Using RANSAC, the instantaneous solutions of  $\Delta \hat{\mathbf{U}}$  and  $\Delta \hat{\mathbf{b}}_i$  can be used to calculate  $\epsilon_i^{j,k,l}(t)$  in Equation 3.7.<sup>50</sup> Because the instantaneous solutions include error contributions from other satellites, the  $\epsilon_i^{j,k,l}(t)$  error includes contributions from other satellites too. The statistic characteristics of  $\epsilon_i^{j,k,l}(t)$  can be used to determine how well  $\Delta f_{i,SV}^{j,k,l}$  can be observed.

$$ADR_i^{j,k,l}(t_1) - ADR_i^{j,k,l}(t_0) - corr_{SV} - corr_{geo} + \mathbf{e}_i^j(t_1)\Delta \hat{\mathbf{U}} - \Delta \hat{\mathbf{b}}_i = \Delta f_i^{j,k,l} + \epsilon_i^{j,k,l}(t) \quad (3.7)$$

### 3.4 Using RANSAC with Instantaneous Measurements

An estimate of  $\Delta U$  can be used to observe  $\Delta f_{i,SV}^{j,k,l}$  and  $\epsilon_i^{j,k,l}(t)$  in this work. The term  $\Delta U$  can be reliably estimated from RANSAC. RANSAC can be used to identify outliers in the solution of  $\Delta U$ . This allows for identification of data channels or satellites that are providing the outlier data. These data sources can be excluded from the positioning solution to improve accuracy. To do so, the following algorithm can be applied over  $\kappa$  iterations:<sup>67</sup>

1. For iteration  $\kappa$ ,  $M$  measurements are randomly selected as an initial core set  $s_\kappa^*$ . Since there are four unknowns in the TDCP solution,  $M = 4$  in this case. The initial core set  $s_\kappa^*$  is used to solve for the initial core solution  $\tilde{\mathbf{x}}_\kappa$ . If the solution is erroneous, skip the iteration.
2. Compute the error function  $Err(z_n, \mathbf{H}_n, \tilde{\mathbf{x}}_\kappa)$ . The measurements with an error function smaller than some threshold  $\gamma$  would be considered inliers.
3. Record the size of the set of indices of all inliers in iteration  $\kappa$  as criterion  $C_\kappa$ .
4. If  $C_\kappa$  is greater than the current maximum  $C_{max}$ , solve for  $\hat{\mathbf{x}}_\kappa$  using all the inliers.

Then, record the following parameters:  $\hat{\kappa} = \kappa$ ;  $C_{max} = C_{\kappa}$ ;  $\tilde{\mathbf{x}}_{\hat{\kappa}} = \hat{\mathbf{x}}_{\kappa}$ ;  $\hat{\mathbf{x}}_{\hat{\kappa}} = \hat{\mathbf{x}}_{\kappa}$ ;  $s_{\hat{\kappa}} = s_{\kappa}$ ; and  $s_{\hat{\kappa}}^* = s_{\kappa}^*$ .

The error function  $Err(z_n, \mathbf{H}_n, \tilde{\mathbf{x}}_{\kappa})$  from step 2 will follow a 1-degree of freedom Chi distribution.<sup>67</sup> If the error function is less than the selected  $\gamma$  ( $\gamma = 2$  by default), a fault-free measurement has a 95% chance of falling into a domain  $\mathbf{D}_{\kappa}$  that is based on  $\tilde{\mathbf{x}}_{\kappa}$ , assuming that  $\mathbf{D}_{\kappa}$  is unbiased.<sup>67</sup> The measurements that are not included in  $\mathbf{D}_{\kappa}$  are part of the inlier set. If a large portion of the measurements are fault-free, they will agree with each other when compared to an unbiased  $\mathbf{D}_{\kappa}$ . With RANSAC, a majority of the measurements are not required to be fault-free; it only needs at least one fault-free core solution through the  $\kappa$  iterations to form a valid solution.<sup>67</sup> The likelihood of RANSAC failure for different levels of faulty measurements and the overall effectiveness of the algorithm is further explored in Zhu et al.<sup>66</sup>.

### 3.5 Simulated Bias in Satellite Orbit

As described in Section 2.2, the different sources of error would manifest as biases of different orders in TDCP. As previously mentioned, the atmospheric effects would manifest as a zeroth-order bias in TDCP.<sup>29</sup> The difference between the real-time residuals and the SP3-corrected residuals may aggregate over time and appear as a first-order bias in TDCP.<sup>29</sup> Under normal operations for GPS, the drift is expected be less than  $0.006 \text{ m/s}$ .<sup>44</sup>

For a more controlled test, first-order biases of different levels were added to the the existing data for satellite 14 to simulate a greater drift in satellite orbit. The bias started 20% of the way into the whole data set and increased linearly with a defined slope. The downsampling and thresholding analysis was re-accomplished on the residuals with added simulated biased. The following slopes were used:  $1 \times 10^{-4}$ ,  $5 \times 10^{-5}$ ,  $1 \times 10^{-5}$ ,  $5 \times 10^{-6}$ ,  $1 \times 10^{-6}$ ,  $5 \times 10^{-7}$ , and  $1 \times 10^{-7}$ . The smaller slopes represented nominal errors, while the

larger slopes represented phenomena like faults, broadcast errors, spoofing, etc.

### 3.6 Downsampling and Thresholding

The SP3-corrected data was divided into “windows” containing the following number of points in each window: 10, 25, 50, 60, 75, 100, 150, 250. Note that there is one point every second, so the window size can also be considered temporally (*i.e.*, 10 *s*, 25 *s*, 50 *s*, 60 *s*, 75 *s*, 100 *s*, 150 *s*, 250 *s*). The mean of each window was used to downsample the data.

The residuals were not assumed to be independent over time and identically distributed, nor were they assumed to be Gaussian, so standard deviation would not serve as a valid metric. One way to evaluate temporal correlation is autocorrelation. Autocorrelation evaluates how closely points are statistically related.<sup>55</sup> The autocorrelation of white noise (which is analogous to an independent and identically distributed continuous functions) would be a single spike.<sup>53</sup> If there was a peak with a finite width in the resulting data, there was some sort of statistical dependence between the points, thereby validating the assumption that the residuals were not independent and identically distributed. The peak halfwidth identifies the time lag in the autocorrelation.<sup>6</sup> The time lag may be helpful in determining ideal window sizes for analysis.

Another method of analyzing time-variant data to identify stochastic processes is the Allan variance described in Section 2.6. The Allan variance was calculated for satellite 14 and satellite 31 following the process described in Shah et al.<sup>50</sup>

The initial windows were used to calculate thresholds that was the mean of those downsampled window means and three times their RMS.<sup>29</sup> The number of initial windows selected were: 3, 5, 10, 15, 20, and 25. Any downsampled window that had an average value that was more than three times the RMS away from the mean of the initialization period was flagged as an outlier. Since each combination of initialization period and window size had

a different number of points, comparing the number of outliers was not a valid comparison. Instead, the percentage of points identified as outliers was used as the metric for analysis.

# Chapter 4

## Results and Analysis

### 4.1 SP3 Corrections

Two satellites were chosen for initial analysis, since they were in view for the majority of the flight. The original residuals for satellite 14 and 31 are illustrated in Figure 4.1 and Figure 4.2. Also illustrated on those figures are the residuals with the SP3 corrections applied and the difference between the two measurements for each satellite. The summary statistics for the difference between the original and SP3-corrected residuals are summarized in Table 4.1

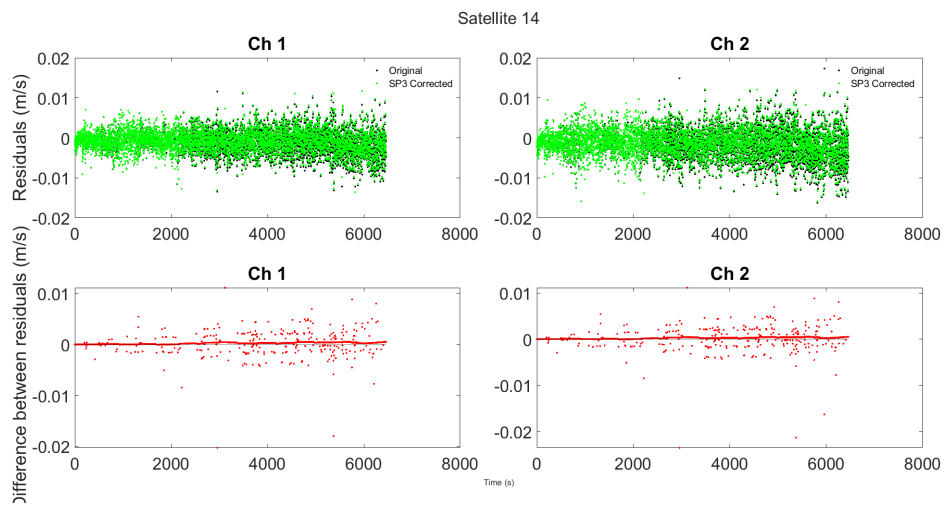


Figure 4.1: Comparison of original and SP3-corrected residuals for satellite 14

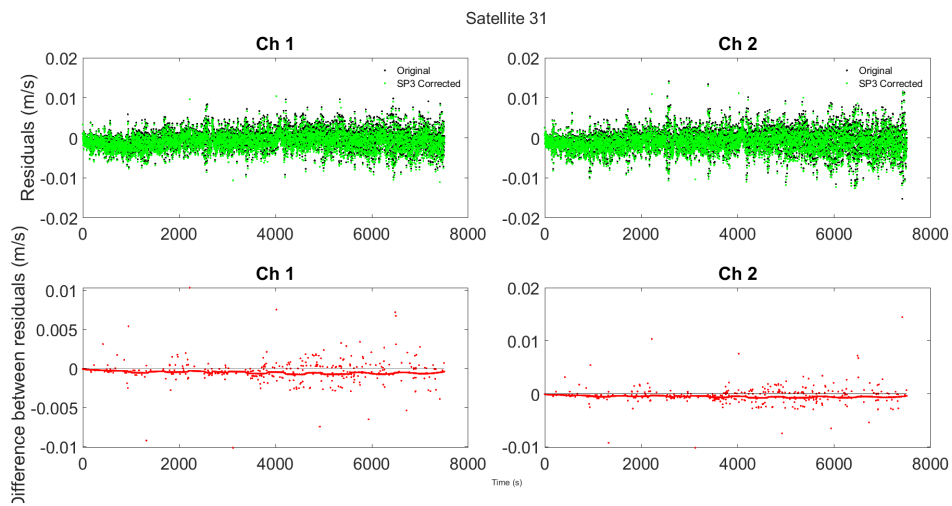


Figure 4.2: Comparison of original and SP3-corrected residuals for satellite 31

Table 4.1: Summary statistics of differences between original and SP3-corrected residuals

Satellite	Channel	Mean	Standard Deviation
14	1	$2.44 \times 10^{-4}$	$6.54 \times 10^{-4}$
	2	$2.40 \times 10^{-4}$	$7.15 \times 10^{-4}$
31	1	$-5.05 \times 10^{-4}$	$4.08 \times 10^{-4}$
	2	$-5.03 \times 10^{-4}$	$4.41 \times 10^{-4}$

The two channels ( $L1$ ,  $L2$ ) in each satellite had approximately equivalent performance, as summarized in Table 4.1. This makes logical sense, since the signals were following almost the exact same path from satellite to receiver and were thus subject to the same conditions along the way. As seen in Figure 4.2, both channels in satellite 31 had a growing bias between the original measurements and the SP3 corrections. The increasing bias in satellite 31 resulted in a mean value ( $-5.05 \times 10^{-4}$  for channel 1 and  $-5.03 \times 10^{-4}$  for channel 2) that has a greater magnitude than that of satellite 14.

## 4.2 Autocorrelation

Figure 4.3 illustrates the autocorrelation for the residuals from satellite 14. There was a

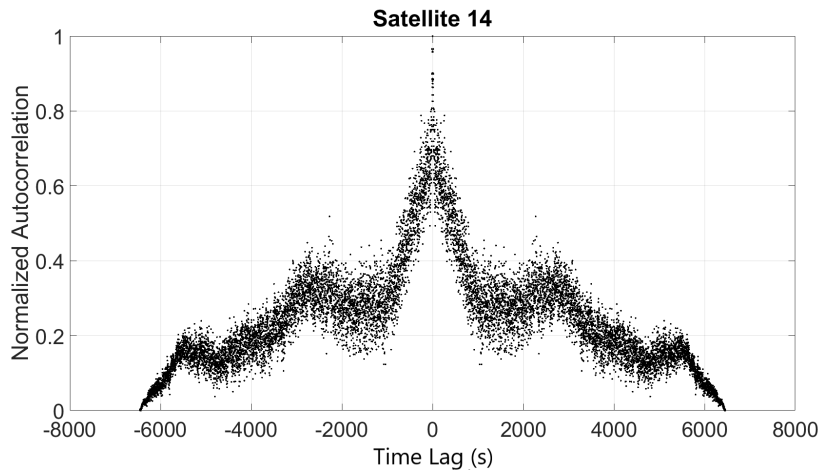


Figure 4.3: Normalized autocorrelation for satellite 14

peak that did not resemble an impulse function (*i.e.*, there was not a single spike), indicating

that the residuals were not independent over time. The primary peak in Figure 4.3 is highlighted in Figure 4.4.

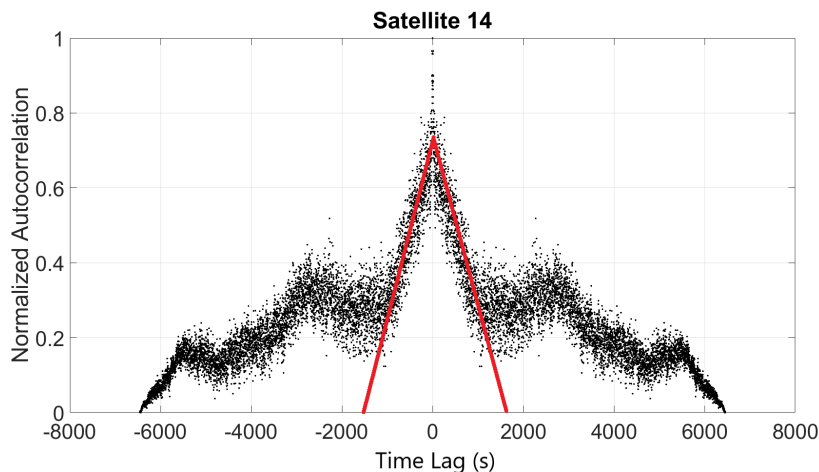


Figure 4.4: Normalized autocorrelation for satellite 14 with primary peak highlighted

The base of the peak was approximately 1800 s indicated there was a statistical dependence in points with a time constant on the scale of several hundred seconds . A time constant on that scale suggested that the dependence could be related to motion, position, or orientation (*e.g.*, aircraft flying in a loop that had a 30-*min* orbit). We hypothesize that a signal-related autocorrelation would have had a time constant the order of seconds or even sub-second.

Figure 4.5 illustrates the autocorrelation for the residuals from satellite 31. The primary and secondary peaks in Figure 4.5 are highlighted in Figure 4.6.

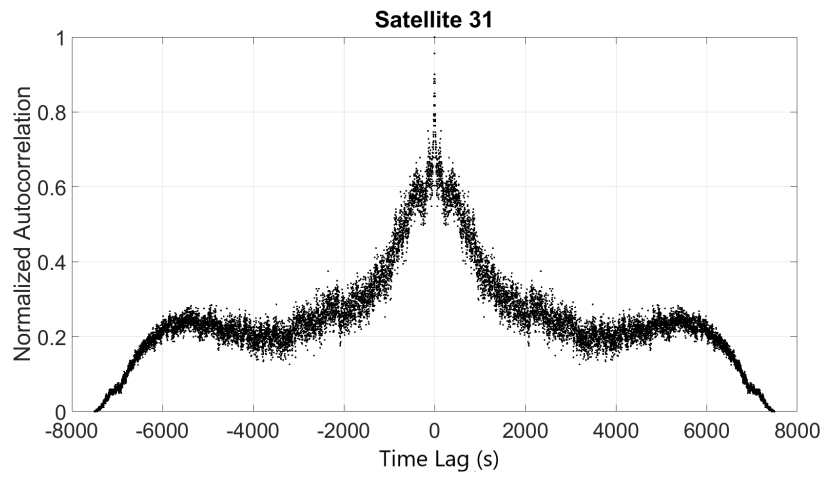


Figure 4.5: Normalized autocorrelation for satellite 31

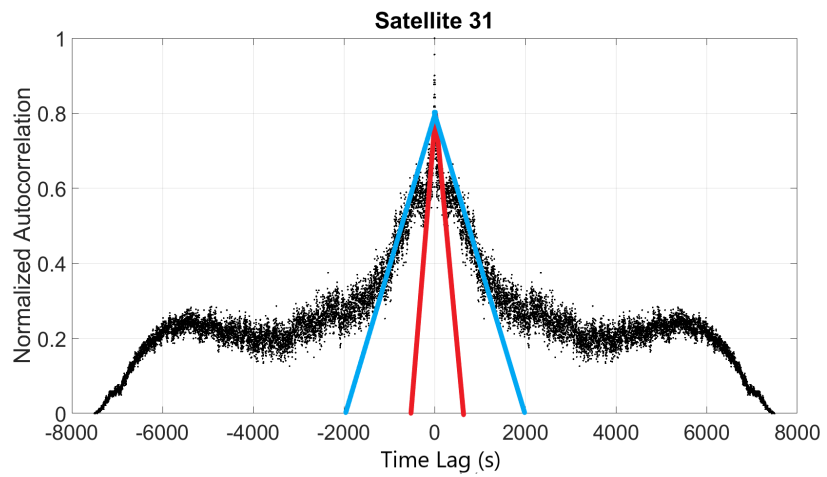


Figure 4.6: Normalized autocorrelation for satellite 31 with primary (red) and secondary (blue) peaks highlighted

The primary base of the peak of approximately 500  $s$  indicated there was a statistical dependence in points with a time constant on the scale of several hundred seconds. A time constant on that scale suggested that the dependence could be related to motion, position, or orientation (*e.g.*, aircraft flying in a loop that had an 8-*min* orbit). We hypothesize that a signal-related autocorrelation would have had a time constant on the order of seconds or even sub-seconds. The secondary base of the peak was approximately 2000  $s$  (or 33 *min*), which is similar to the time constant from satellite 14 of 1800  $s$  (or 30 *min*). It is likely that both time constants were identifying the same phenomenon.

The overall shape of the autocorrelation of both satellites was approximately triangular, which suggested the distribution approximated a Gauss-Markov process. They may be related to residual errors in the estimated solution or satellite geometry.

### 4.3 Allan Variance

The relationship between Allan variance ( $\sigma_{AV}$ ) and the cluster length ( $\tau$ ) for satellite 14 is illustrated in Figure 4.7. The slope of the best fit line describes the trend, based on Table 2.2. The first segment had a slope of -0.207 and the second segment had a slope of 0.603. The first slope indicated the presence of a correlated noise process, while the second slope suggested either white noise or a time-differenced random walk trend. However, based on the autocorrelation results, there was not pure white noise present. Additionally, since the initial residuals were time-differenced, the time-differenced random walk was more likely to be process that was present.

The Allan variance had a minimum value around a time constant of  $\tau = 200$   $s$ . Therefore, to minimize the impact of stochastic processes, the residuals should be averaged at approximately 200  $s$  intervals.<sup>19</sup>

There was a distinct pattern in the Allan variance results around a time constant of

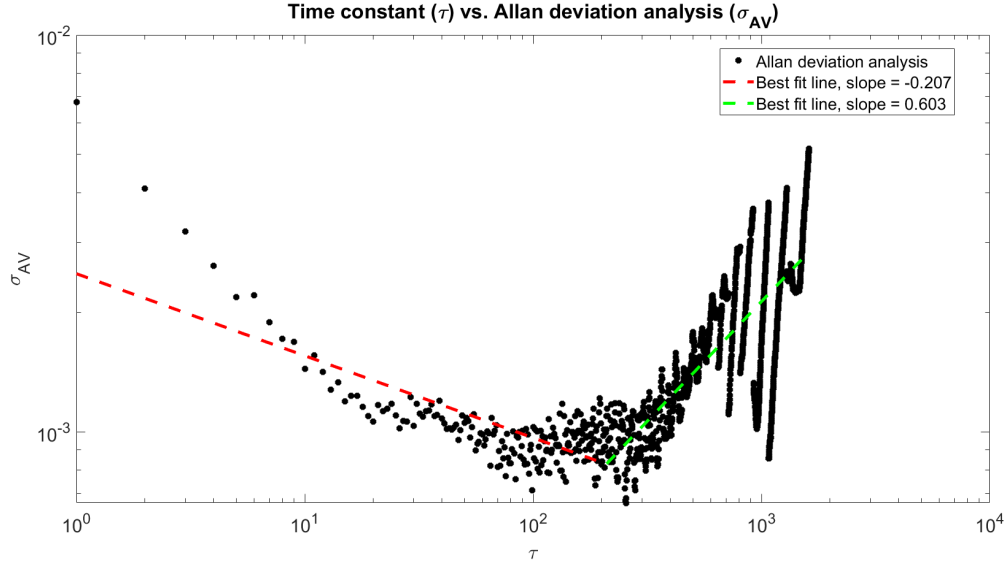


Figure 4.7: Allan variance analysis for satellite 14

$\tau = 10^3 \text{ s} = 1000 \text{ s}$ , which was on the same order of magnitude as the 1800 s halfwidth of the autocorrelation peak of satellite 14. Therefore, the Allan variance analysis was likely identifying the same effects from the autocorrelation analysis illustrated in Figure 4.4.

The relationship between Allan variance ( $\sigma_{AV}$ ) and the cluster length ( $\tau$ ) for satellite 31 is illustrated in Figure 4.8.

The first segment had a slope of -0.218 and the second segment had a slope of 1.057. The first slope indicates the presence of a correlated noise process, similar to the results of satellite 14 in Figure 4.7. The second slope also suggests either white noise or a time-differenced random walk trend.

The Allan variance had a minimum value around a time constant of  $\tau = 400 \text{ s}$ . To minimize the impact of stochastic processes, the residuals should be averaged at approximately 400 s intervals.<sup>19</sup>Overall, the Allan variance analysis for satellite 31 agreed with the results of satellite 14.

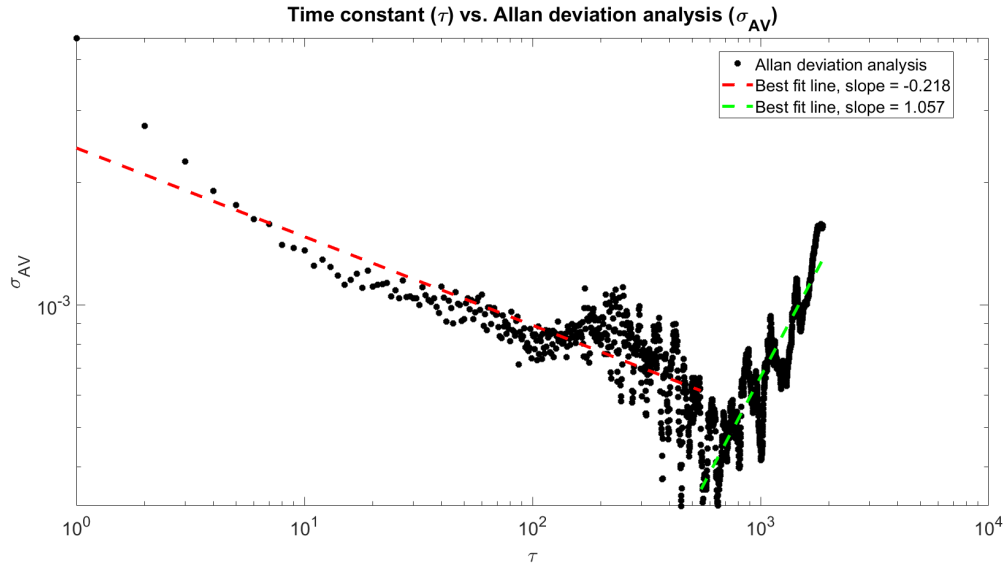


Figure 4.8: Allan variance analysis for satellite 31

## 4.4 Elevation Angle

The carrier-to-noise ratio  $C/N_0$  is affected by the elevation angle between the satellite and the user, since the signal interacts with more of the atmosphere at low elevation angles of  $15^\circ$  or lower.<sup>29</sup> The elevation angle for the duration of the flight for satellite 14 is illustrated in Figure 4.9.

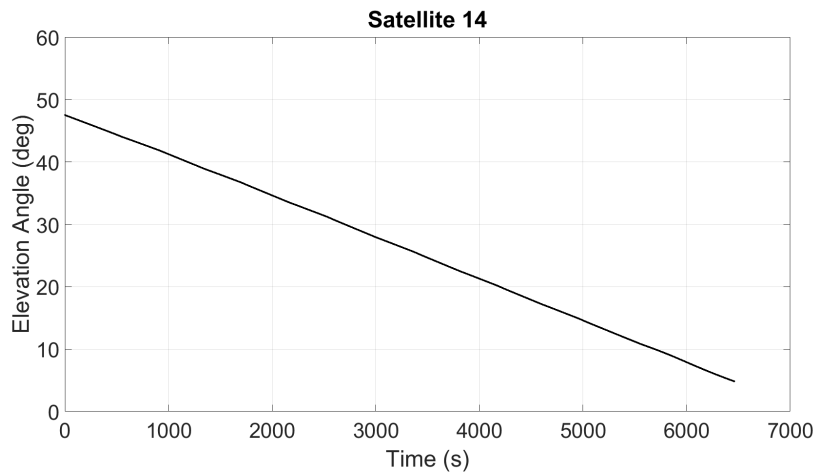


Figure 4.9: Elevation angle of satellite 14

The elevation angle fell below  $15^\circ$  about  $5000\text{ s}$  ( $83\text{ min}$ ) into the flight. Since both channels in satellite 14 had similar results, channel 1 was used for further analysis of the effect of elevation angle. The corrected residuals from channel 1 from Figure 4.1 are reproduced in Figure 4.10 with the addition of a 250-point centered moving average. Figure 4.10 with an approximation of the moving average line is illustrated in Figure 4.11.

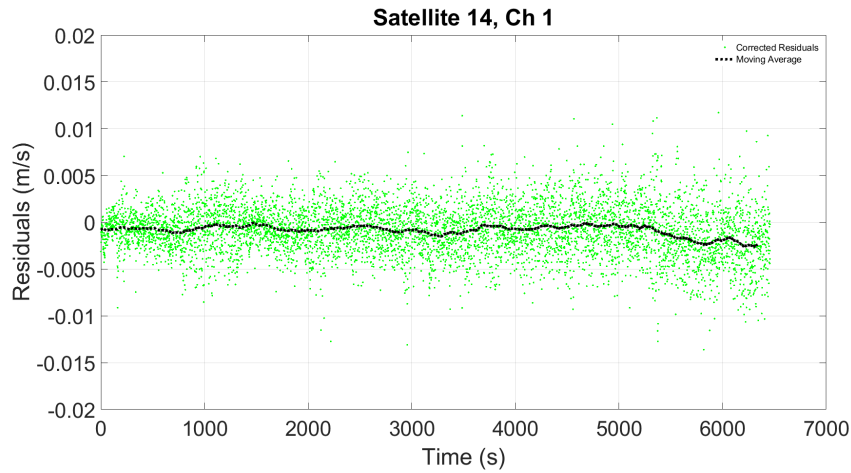


Figure 4.10: Corrected residuals from satellite 14, channel 1 with a 250-point centered moving average

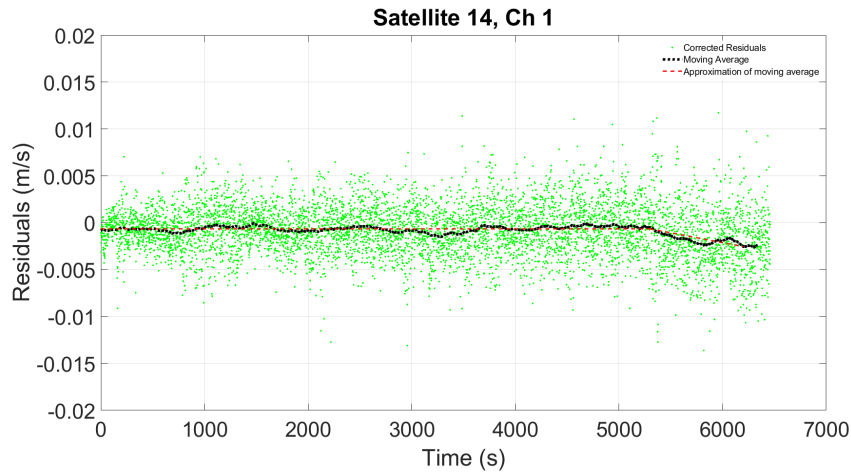


Figure 4.11: Corrected residuals from satellite 14, channel 1 with a 250-point centered moving average and approximation of the moving average

There was a noticeable change in the slope around the  $5300\text{ s}$  mark, resulting in a

first-order bias with slope of approximately  $-2 \times 10^{-6} \frac{m/s}{s}$ . Prior to the 5300 s mark, the moving average appeared to identify a zeroth-order bias (*i.e.*, approximately constant value) of  $-6.5 \times 10^{-4}$ , though there was some observable sinusoidal noise. The simultaneity of the low elevation angle and change in slope of the residuals suggests there may have been a causal relationship between the two. In an operational case, users would likely disregard signals from satellites with elevation angles below  $15^\circ$ .

The elevation angle for the duration of the flight for satellite 31 is illustrated in Figure 4.12. The elevation angle falls below  $15^\circ$  about 7500 s (125 min) into the flight. The

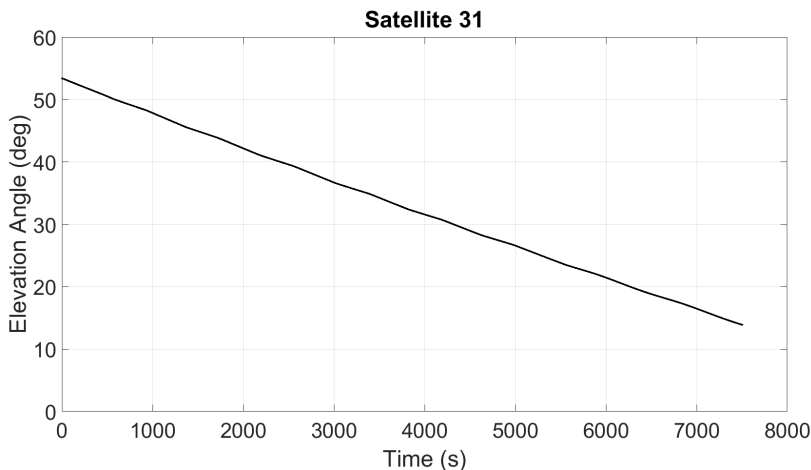


Figure 4.12: Elevation angle of satellite 31

7500 s point also marks the end of the flight, so the low elevation angle did not appear to significantly affect the overall results for satellite 31.

Since both channels in satellite 31 had similar results, channel 1 was used for further analysis of the effect of elevation angle. The corrected residuals from channel 1 from Figure 4.2 were reproduced in Figure 4.13 with the addition of a 250-point centered moving average. Figure 4.13 with an approximation of the moving average line is illustrated in Figure 4.14.

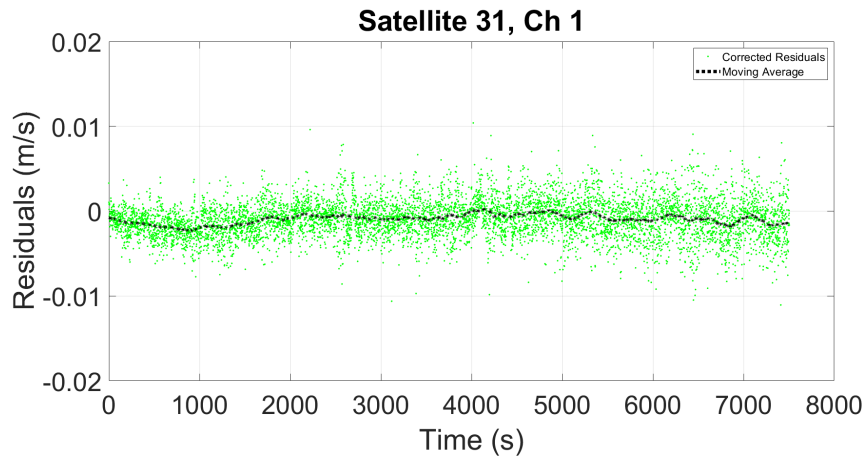


Figure 4.13: Corrected residuals from satellite 31, channel 1 with a 250-point centered moving average

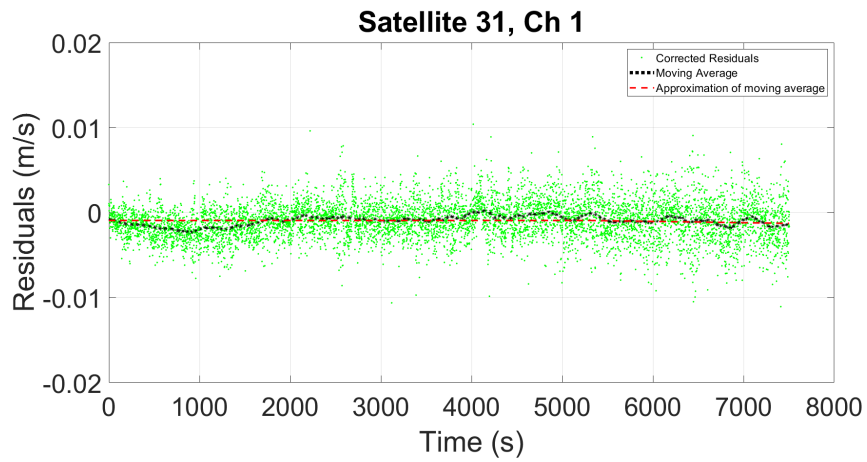


Figure 4.14: Corrected residuals from satellite 31, channel 1 with a 250-point centered moving average and approximation of the moving average

For the first 2000  $s$ , there is a noticeable drop dip the residuals. The decrease and increase are both roughly first-order biases with a slope of approximately  $\mp -2.5 \times 10^{-4}$ , respectively. After to the 2000  $s$  mark, the moving average appears to identify a zeroth-order bias (*i.e.*, approximately constant value) of  $-9.2 \times 10^{-4}$ , though there is some observable sinusoidal noise. Unlike the case with satellite 14, there was sinusoidal noise even when the elevation angle was above  $15^\circ$ .

## 4.5 Autocorrelation of Truncated Data

For a more representative analysis, the residuals from satellite 14 were truncated to 5300  $s$  (*i.e.*, data from the satellite when it was below an elevation angle of  $15^\circ$  were discarded). Figure 4.15 illustrates the recalculated autocorrelation for the truncated residuals from satellite 14. For comparison, both the original and truncated autocorrelation analyses are illustrated

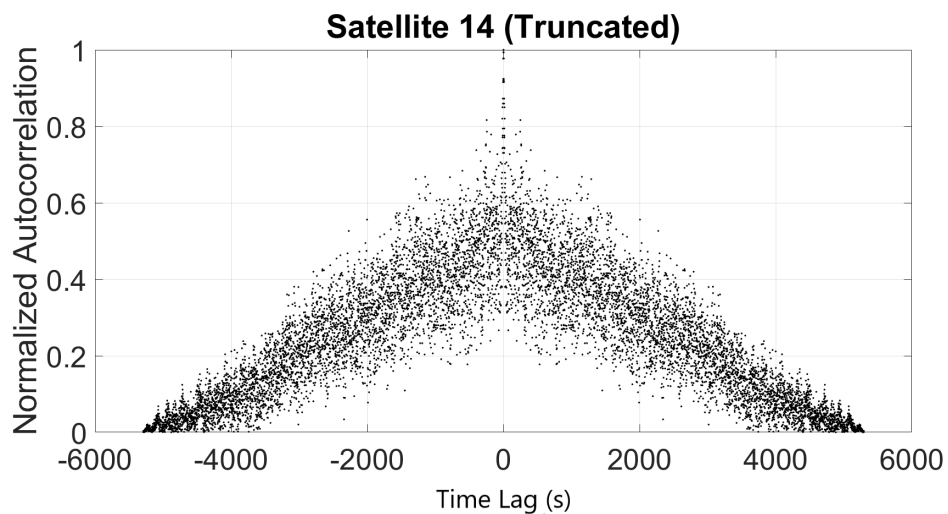


Figure 4.15: Normalized autocorrelation for truncated satellite 14 residuals

in Figure 4.16.

As seen in Figure 4.16, there was not a distinct wide peak in the truncated autocorrelation like there was in the original data. The overall triangle distribution of the autocorrelation

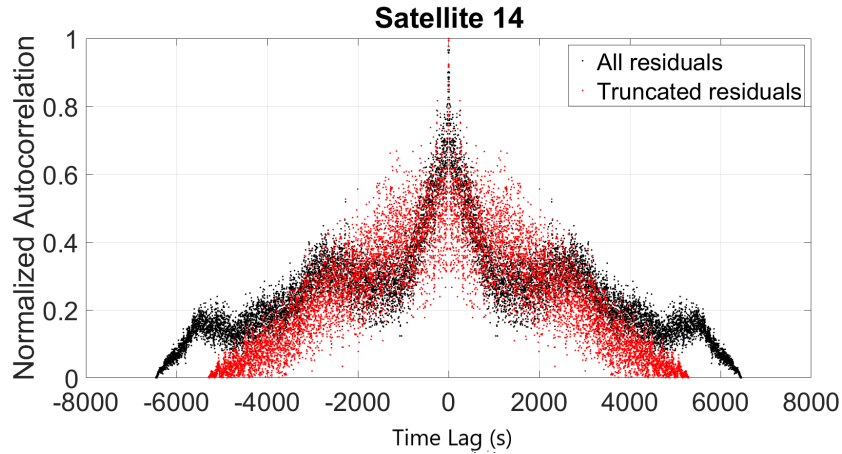


Figure 4.16: Comparison of original residuals and truncated residuals for satellite 14

in Figure 4.15 suggested the truncated residuals better fits a Gaussian distribution, but it still includes a correlation competent.

For the sake of thoroughness, the residuals for satellite 31 were truncated to 6250 s, which was when the satellite fell below 20°. Figure 4.17 illustrates the recalculated autocorrelation for the truncated residuals from satellite 31. For comparison, both the original and truncated

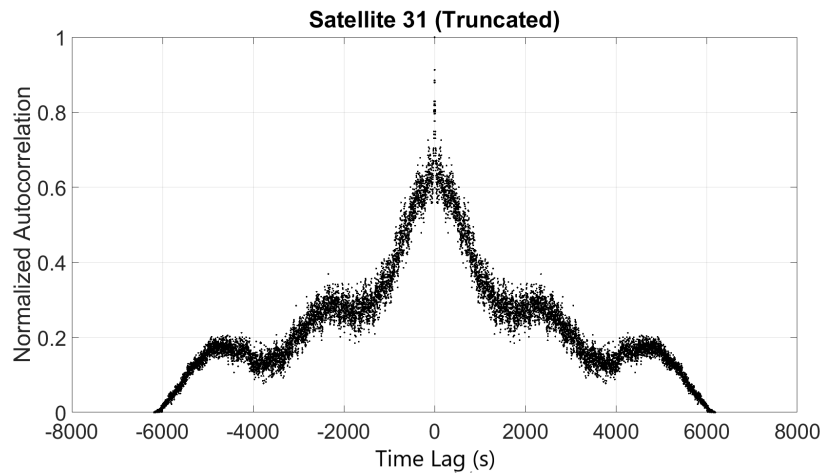


Figure 4.17: Normalized autocorrelation for truncated satellite 31 residuals

autocorrelation analyses are illustrated in Figure 4.18.

As seen in Figure 4.18, there was not a significant difference between the overall shapes of the autocorrelation analysis for the original data and truncated data. The similarities in

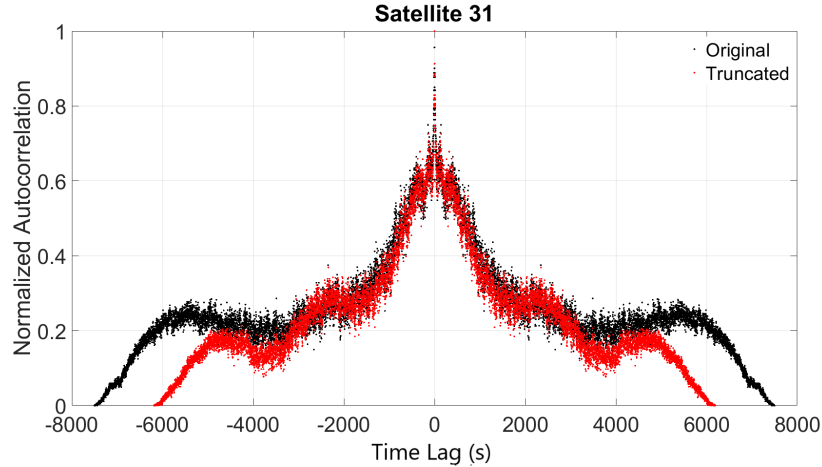


Figure 4.18: Comparison of original residuals and truncated residuals for satellite 31

shape verifies that there were no significant impacts on the autocorrelation caused by low elevation angle for satellite 31.

## 4.6 Allan Variance Analysis of Truncated Data

Similar to the autocorrelation analysis, the Allan variance analysis was re-accomplished for satellite 14 truncated to 5300 s. The relationship between Allan variance ( $\sigma_{AV}$ ) and the cluster length ( $\tau$ ) for the truncated residuals from satellite 14 is illustrated in Figure 4.19.

The first segment had a slope of -0.285 and the second segment had a slope of 1.896. The first slope indicated the presence of a Gauss-Markov process. The second slope did not identify any stochastic processes. The Allan variance had a minimum value around a time constant of  $\tau = 300$  s. To minimize the impact of stochastic processes, the residuals should be averaged at approximately 300 s intervals.<sup>19</sup>

Notably, the distinct pattern that was present in Figure 4.7 around  $\tau = 10^3$  s was missing in Figure 4.19. Therefore, the low elevation angle caused the distinct pattern. Likewise, the autocorrelation results in Figure 4.15 were also missing the identified spike from Figure 4.3, validating the previous conclusion that the Allan variance analysis was identifying the same

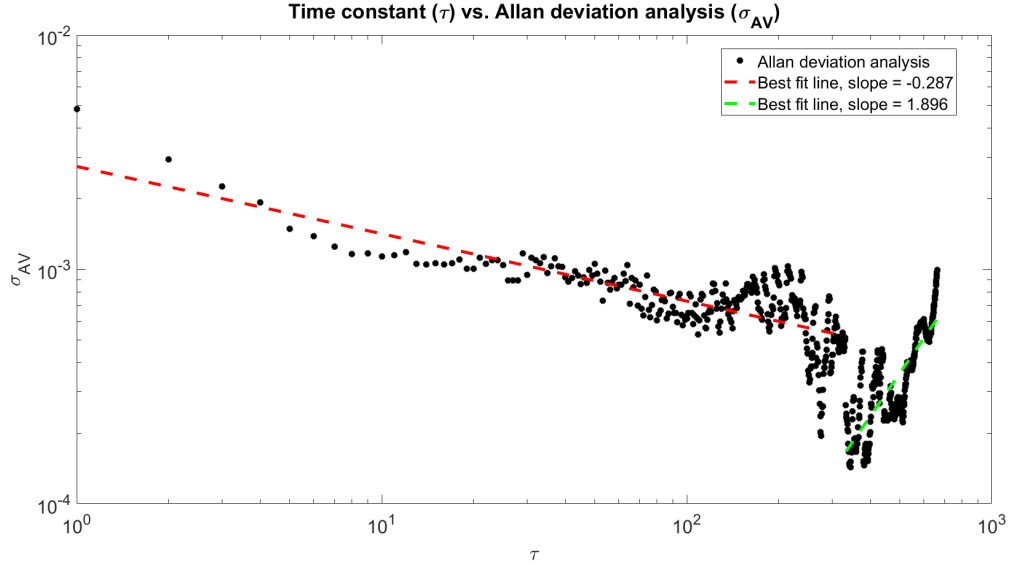


Figure 4.19: Allan variance analysis for truncated residuals from satellite 14

phenomenon as as the autocorrelation analysis.

The autocorrelation results in Figure 4.15 suggested the truncated residuals included random Gaussian noise. The Allan variance analysis suggested the presence of a correlated noise process. The truncated residuals may have a mix of Gaussian noise and a Gauss-Markov process. However, since the time constant was large, the stochastic process could also be modeled as a random walk process. Time differencing each successive data point would lead to a Gaussian distribution. If the differencing occurred at a different interval, the result would be a Gauss-Markov process. Either way, both distributions are Gaussian in nature, so the assumption that the residuals were independent over time was valid.

Since the measurements had been time-differenced, we did not expect to see time-correlated noise of measurements. Additionally, errors caused by tropospheric effects were minimized in the truncated data set. It was more likely that the majority of the errors were related to aircraft motion, position, orientation, and solution. Errors in  $\Delta\hat{U}$  (from Equation 3.7) could be correlated over time, which could be responsible for the correlated noise

components.

The relationship between Allan variance ( $\sigma_{AV}$ ) and the cluster length ( $\tau$ ) for the truncated residuals from satellite 31 is illustrated in Figure 4.20. The first segment had a slope of -0.218

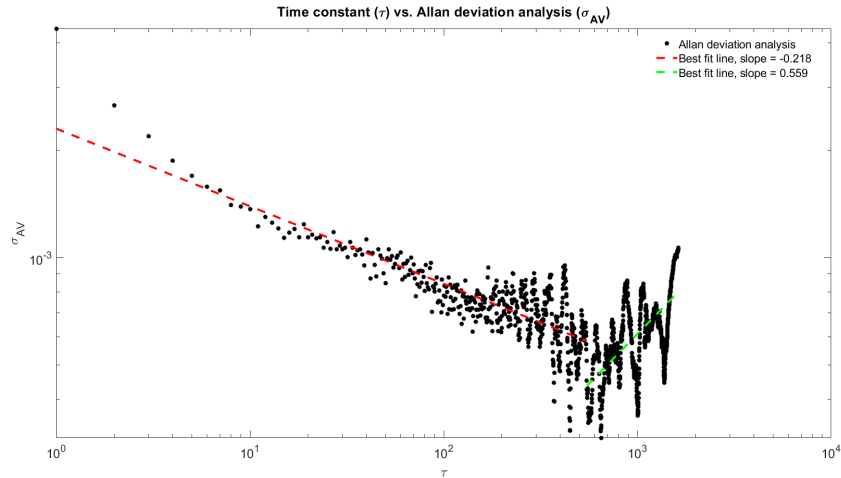


Figure 4.20: Allan variance analysis for truncated residuals from satellite 31

and the second segment had a slope of 0.559. The first slope matched the slope from the Allan variance analysis for the original data and also suggested the presence of a correlated noise process. The second slope suggested the presence of a time-differenced random walk process, similar to the original analysis. The Allan variance had a minimum value around a time constant of  $\tau = 500$  s, versus  $\tau = 400$  s for the original analysis. To minimize the impact of stochastic processes, the residuals should be averaged at approximately 500 s intervals.<sup>19</sup>

Overall, the analysis for the truncated data for satellite 31 matched the original analysis. Additionally, the identified processes in satellite 31 agreed with the results from satellite 14.

## 4.7 Downsampling and Thresholding

Residual errors were downsampled to reduce the impact of error correlation. The SP3-corrected residuals for satellite 14 were downsampled at various rates (“window sizes”). The mean and RMS deviation of the first “initialization period” windows were used to establish thresholds to flag subsequent windows as potential outliers. Note that these outliers are not necessarily erroneous; rather, they are outlier points that may merit further investigation. Points were flagged as outliers if they were more than three times the RMS from the mean. The different combinations of window size and number of initialization periods are illustrated in Figure 4.21 and Figure 4.22, with the outliers flagged with red circles.

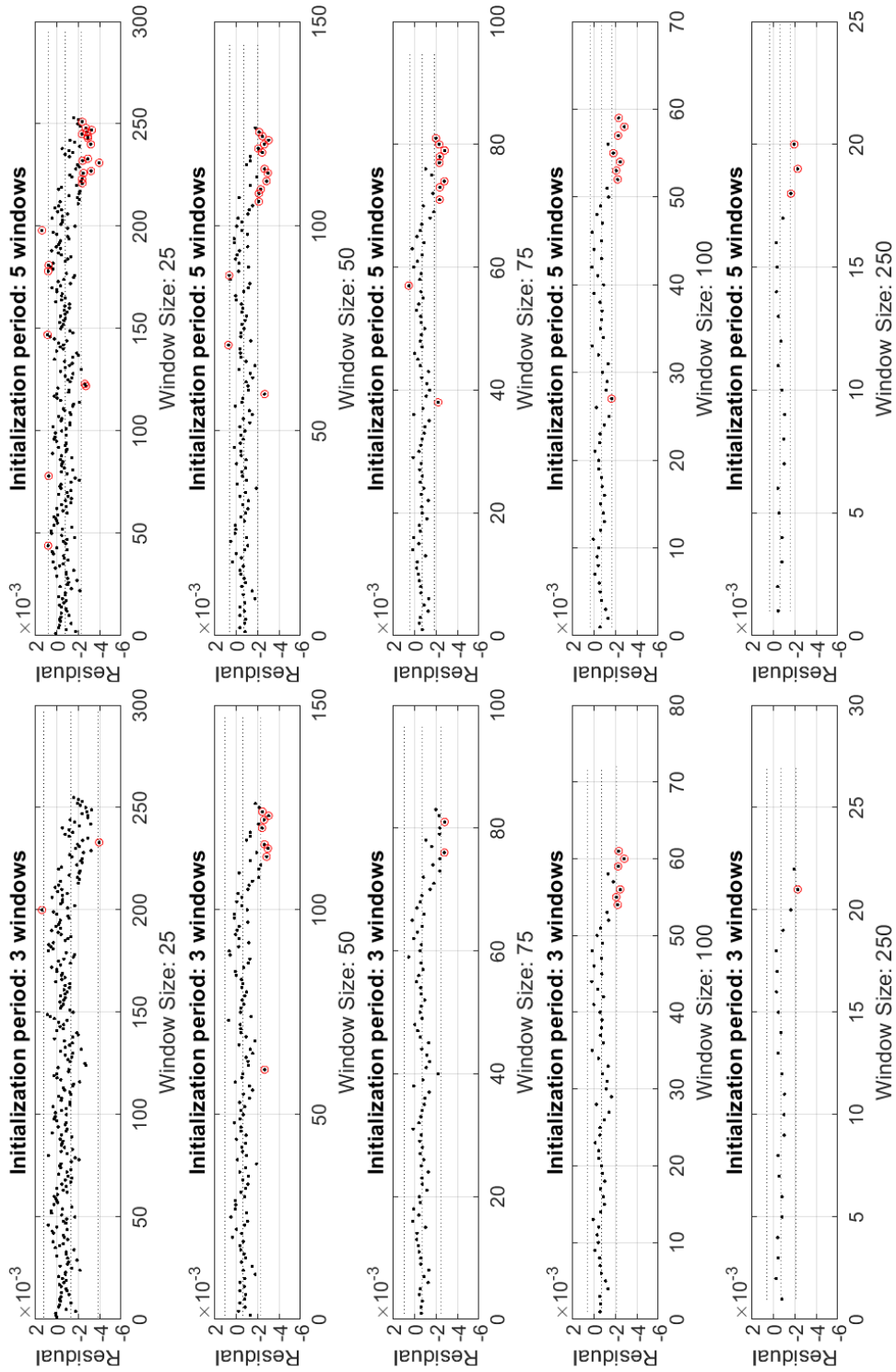


Figure 4.21: Variation of initialization and window sizes for satellite 14, Part A

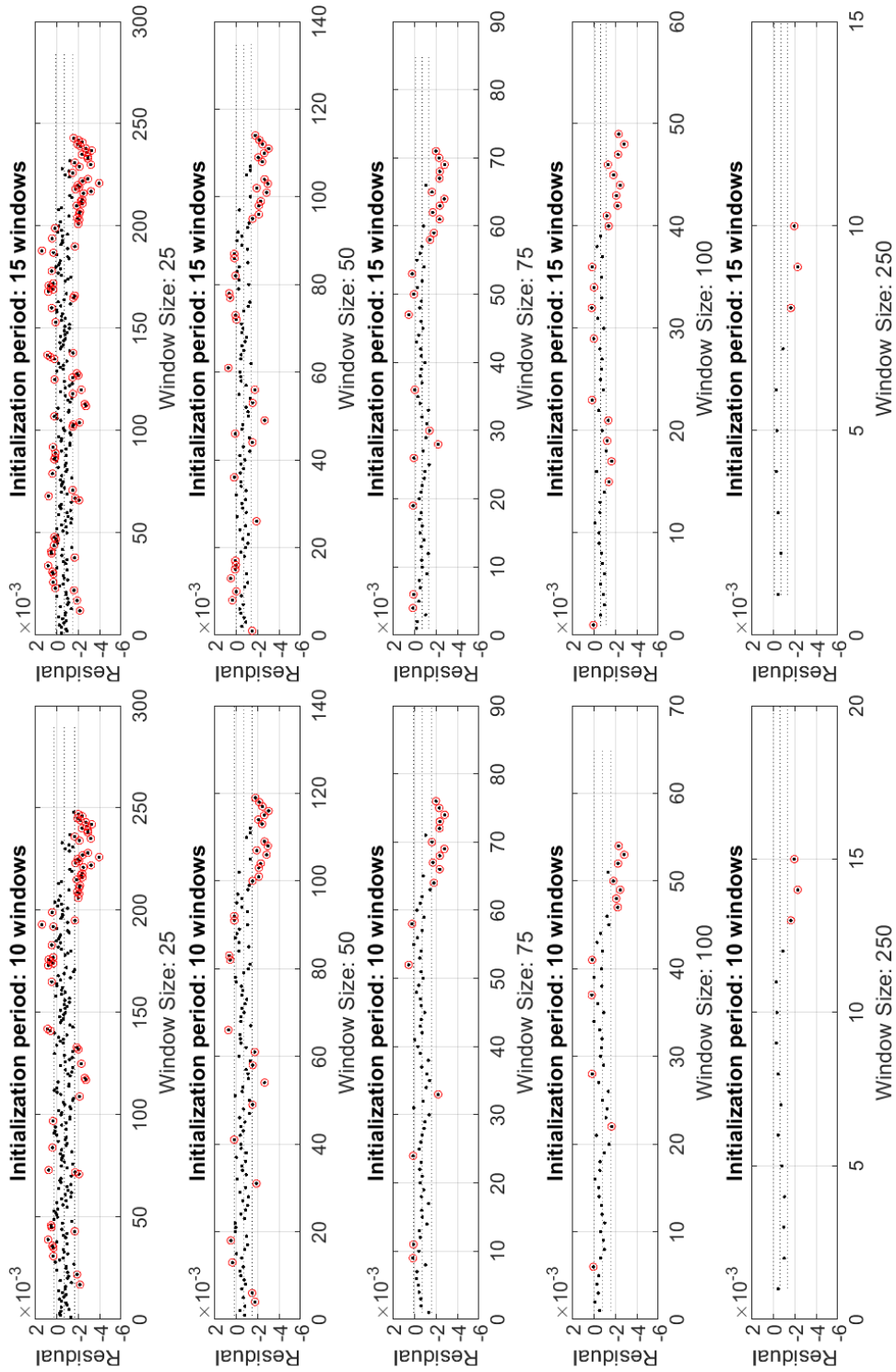


Figure 4.22: Variation of initialization and window sizes for satellite 14, Part B

Since each combinations of initialization period and window size had a unique number of data points, counting just the number of flagged outliers was not a representative measurement. Instead, the percentage of total points flagged as outliers was compared to measure effectiveness, as illustrated in Figure 4.23 and Figure 4.24.

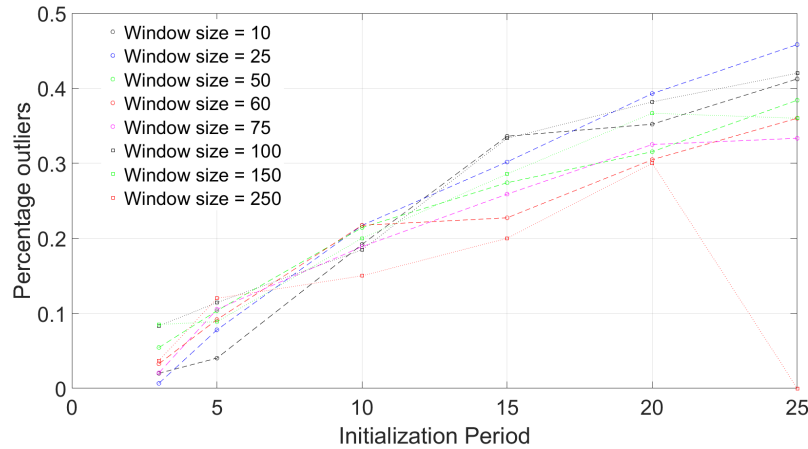


Figure 4.23: Percentage of points identified as outliers versus initialization period

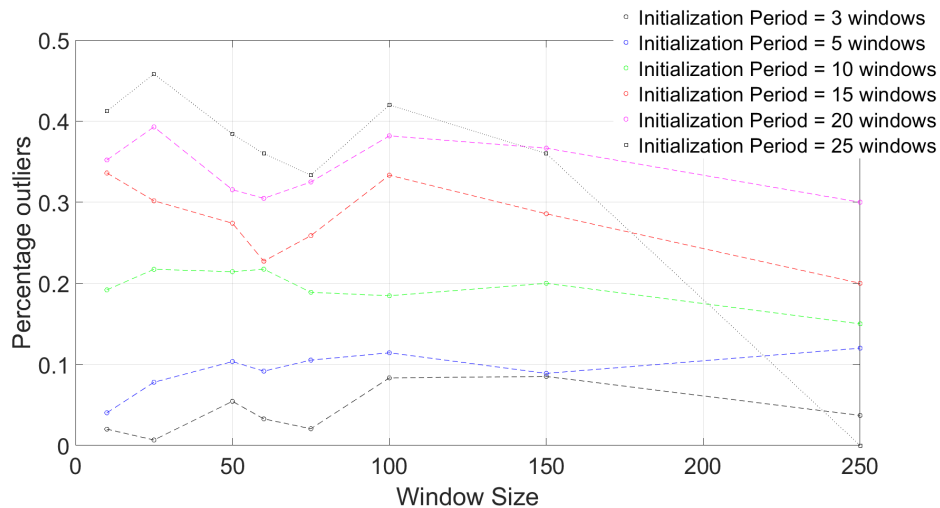


Figure 4.24: Percentage of points identified as outliers versus window size

As seen in Figure 4.23, the percentage of identified outliers increased with a larger initialization period. From the Allan variance analysis, one of the key window sizes identified was 250 s. There were no outliers identified with a window size of 250 s with an initialization

period of 25 windows, since almost all of the points fell within the initialization period. As seen in Figure 4.24, there was not significant variation over the different window sizes for each of the different selected initialization periods. The combination of a window size of 25 *s* and an initialization period of 25 windows appeared to identify the most outliers. This translated to a total of 625 *s* or 10.4 *min* of total initialization time.

The different combinations of window size and number of initialization periods for satellite 31 are illustrated in Figure 4.25 and Figure 4.26, with the outliers flagged with red circles.

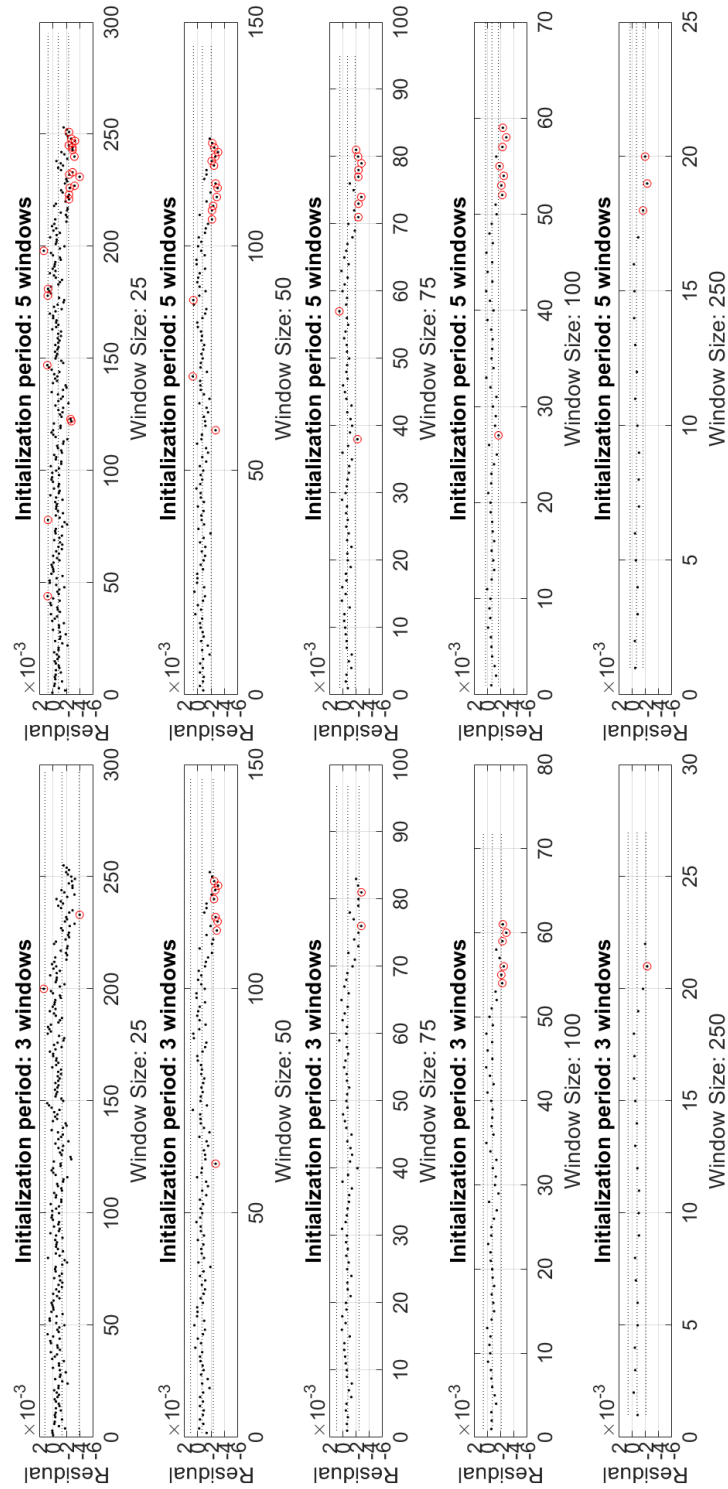


Figure 4.25: Variation of initialization and window sizes for satellite 31, Part A

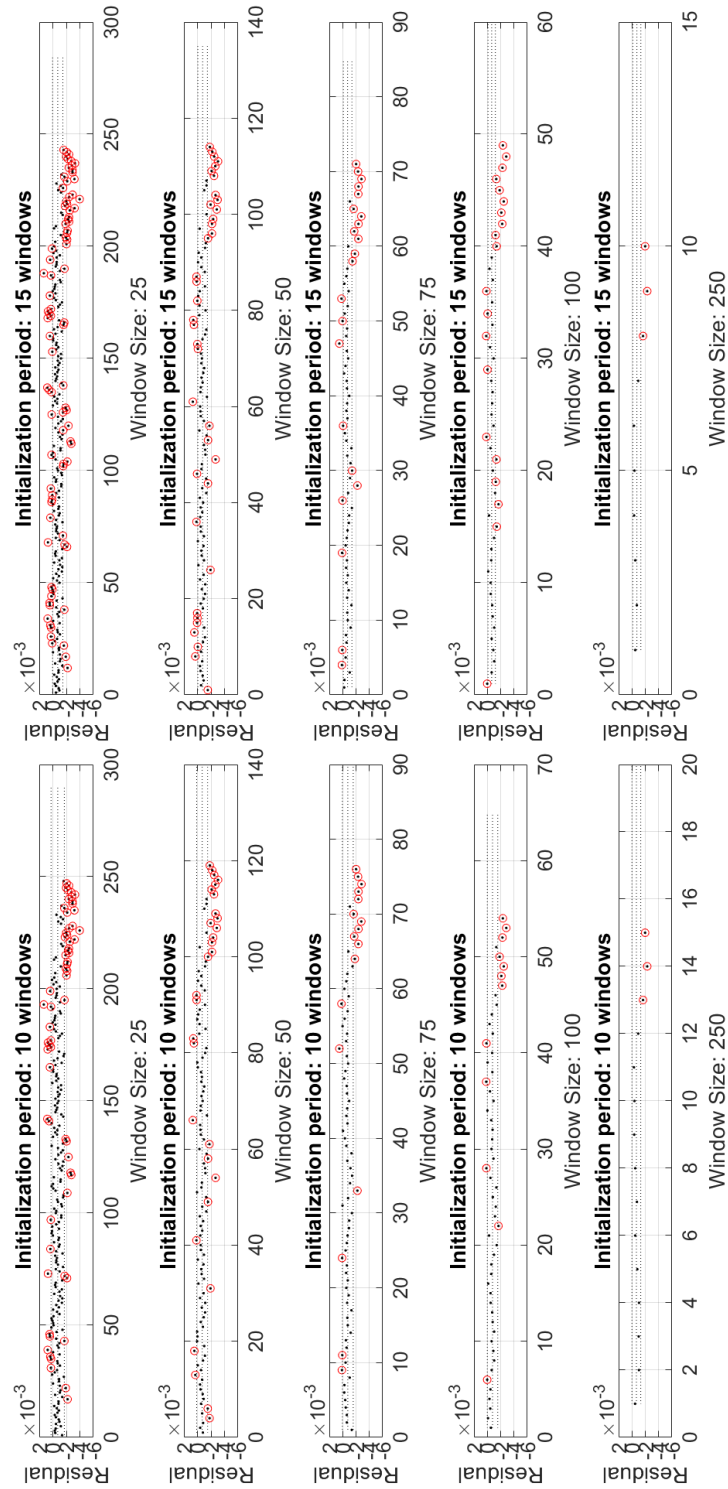


Figure 4.26: Variation of initialization and window sizes for satellite 31, Part B

The percentage of total points flagged as outliers was compared to measure effectiveness, as illustrated in Figure 4.27 and Figure 4.28.

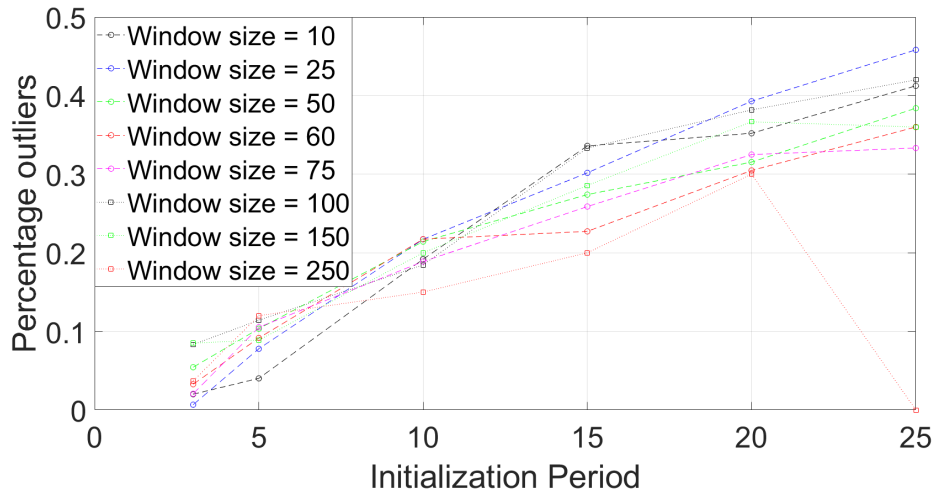


Figure 4.27: Percentage of points identified as outliers versus initialization period

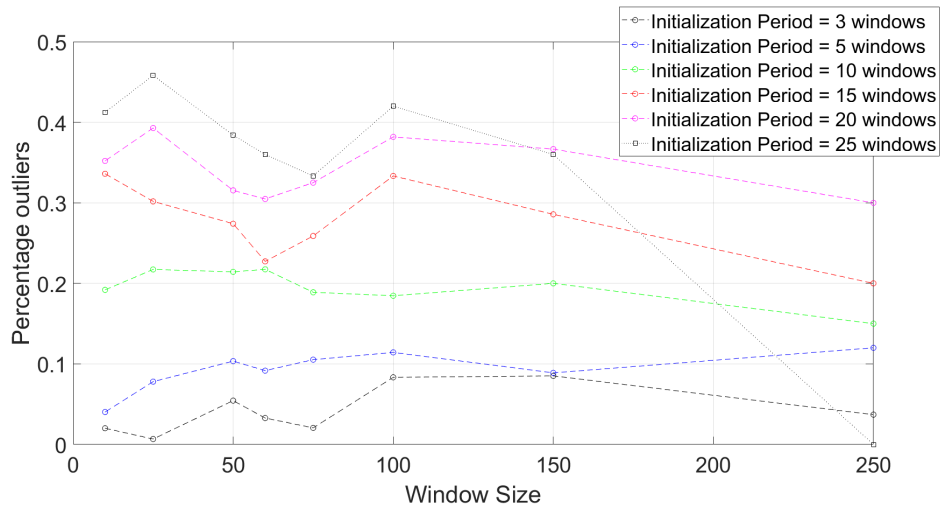


Figure 4.28: Percentage of points identified as outliers versus window size

As seen in Figure 4.27, the percentage of identified outliers increased with a larger initialization period. Like with satellite 14, there were no outliers identified when the case of a window size of 250 *s* with an initialization period of 25 windows since almost all of the points fell within the initialization period. As seen in Figure 4.28, there was not significant

variation over the different window sizes for each of the different selected initialization periods. The combination of a window size of 25 *s* and an initialization period of 25 windows appeared to identify the most outliers. This translated to a total of 625 *s* or 10.4 *min* of total initialization time.

The results in Figure 4.27 and Figure 4.28 agree with the results for satellite 14 from Figure 4.23 and Figure 4.24.

## 4.8 Simulated Bias in Satellite Orbit

The difference between the original and SP3-corrected residuals is illustrated in the bottom two plots of both Figure 4.1 and Figure 4.2. There was a slight bias evident in Figure 4.2; however, for a more controlled test, the simulated first-order biases of different levels were added to the the existing data for satellite 14 to simulate drift. The following slopes were used:  $1 \times 10^{-4}$ ,  $5 \times 10^{-5}$ ,  $1 \times 10^{-5}$ ,  $5 \times 10^{-6}$ ,  $1 \times 10^{-6}$ ,  $5 \times 10^{-7}$ , and  $1 \times 10^{-7}$ .

A subset of the combinations of bias slope, window size, and initialization period are illustrated in Figure 4.29 and Figure 4.30. Note that the size of the window is equal to the time of each cycle (*e.g.*, a window size of 10 means each averaging cycle lasts 10 *s*). The time to identify each simulated bias for each combination of initialization period and window size is summarized in Table 4.2 through Table 4.8.

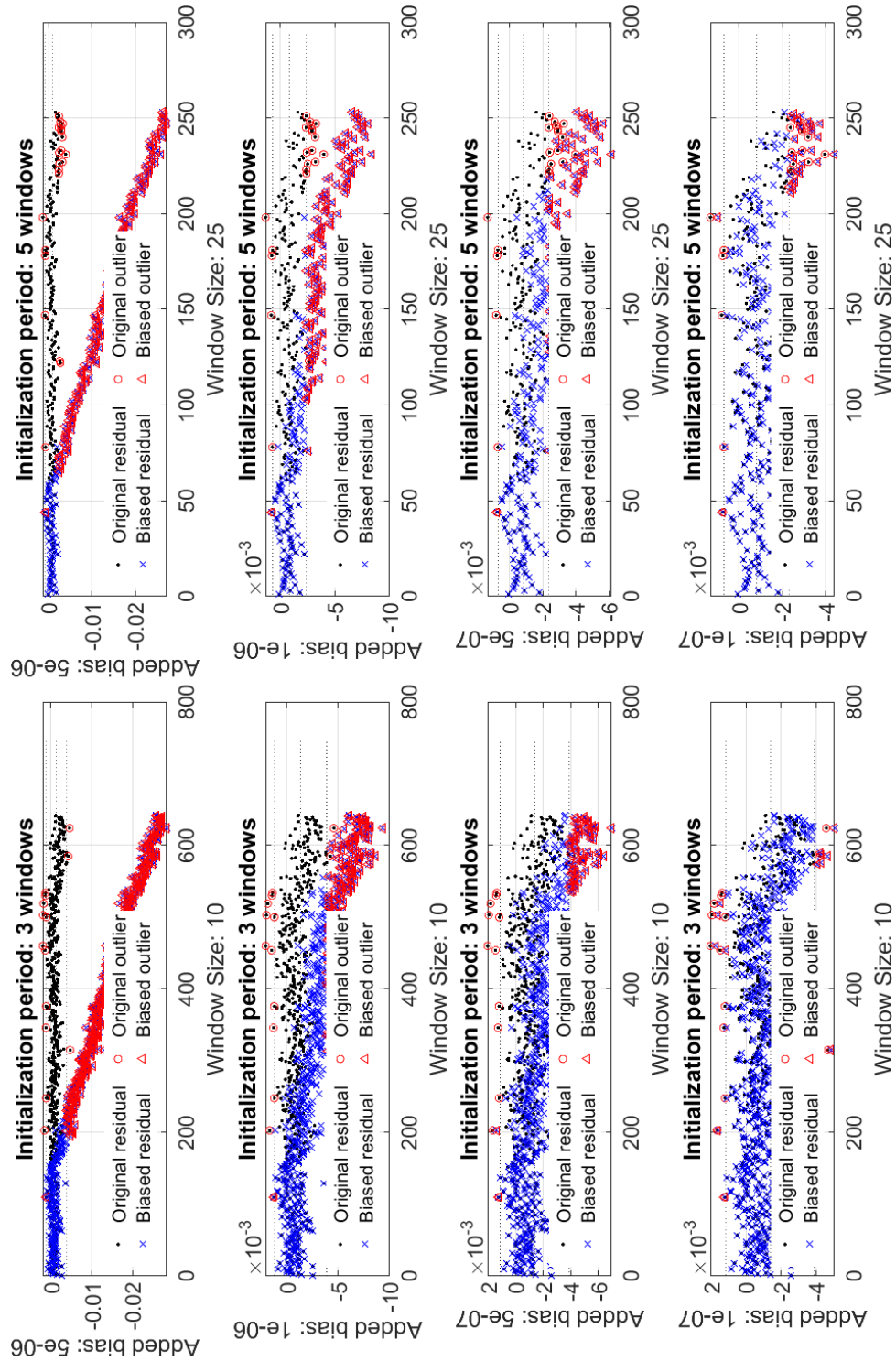


Figure 4.29: Variation of added bias, initialization period, and window size for residuals for satellite 14, Part A

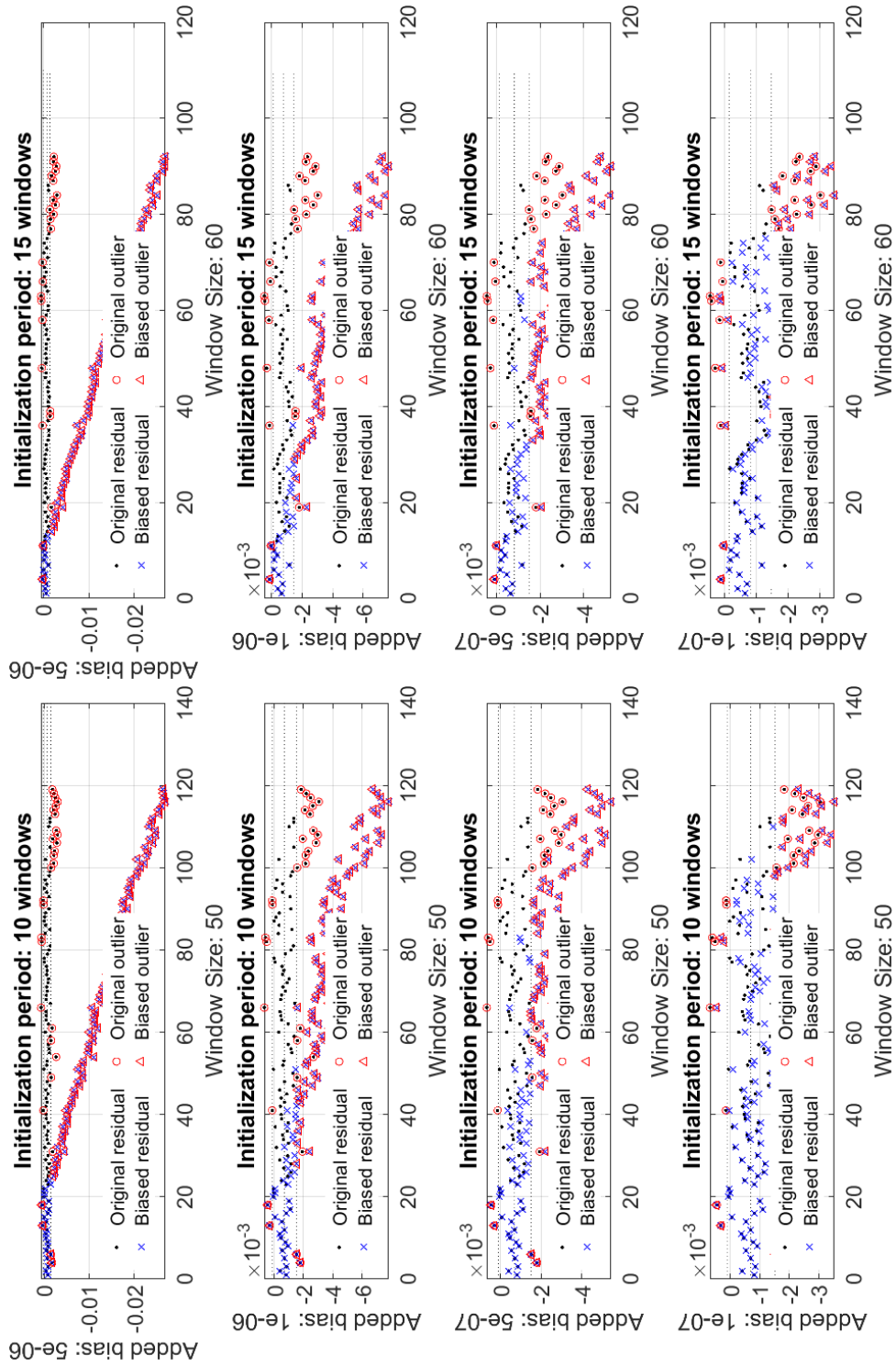


Figure 4.30: Variation of added bias, initialization period, and window size for residuals for satellite 14, Part B

Table 4.2: Time (in  $s$ ) to identify simulated bias of  $1 \times 10^{-4}$

<b>Initialization Period (<math>s</math>)</b>	<b>Window Size (<math>s</math>)</b>							
	<b>10</b>	<b>25</b>	<b>50</b>	<b>60</b>	<b>75</b>	<b>100</b>	<b>150</b>	<b>250</b>
<b>3</b>	50	75	50	60	75	100	150	250
<b>5</b>	50	50	50	60	75	100	150	250
<b>10</b>	30	50	50	60	75	100	150	250
<b>15</b>	30	50	50	60	75	100	150	250
<b>20</b>	30	50	50	60	75	100	150	250
<b>25</b>	30	25	50	60	75	100	150	250

Table 4.3: Time (in  $s$ ) to identify simulated bias of  $5 \times 10^{-5}$

<b>Initialization Period (<math>s</math>)</b>	<b>Window Size (<math>s</math>)</b>							
	<b>10</b>	<b>25</b>	<b>50</b>	<b>60</b>	<b>75</b>	<b>100</b>	<b>150</b>	<b>250</b>
<b>3</b>	90	100	100	120	150	100	150	250
<b>5</b>	90	75	100	120	150	100	150	250
<b>10</b>	60	50	100	120	75	100	150	250
<b>15</b>	30	50	100	120	75	100	150	250
<b>20</b>	30	50	100	60	75	100	150	250
<b>25</b>	30	50	50	60	75	100	150	250

Table 4.4: Time (in  $s$ ) to identify simulated bias of  $1 \times 10^{-5}$

<b>Initialization Period (<math>s</math>)</b>	<b>Window Size (<math>s</math>)</b>							
	<b>10</b>	<b>25</b>	<b>50</b>	<b>60</b>	<b>75</b>	<b>100</b>	<b>150</b>	<b>250</b>
<b>3</b>	270	300	250	240	300	200	300	500
<b>5</b>	270	200	150	180	225	200	300	250
<b>10</b>	140	125	150	180	150	200	300	250
<b>15</b>	110	125	150	180	150	200	150	250
<b>20</b>	110	125	100	120	150	100	150	250
<b>25</b>	100	50	50	60	75	100	150	250

Table 4.5: Time (in  $s$ ) to identify simulated bias of  $5 \times 10^{-6}$

Initialization Period ( $s$ )	Window Size ( $s$ )							
	10	25	50	60	75	100	150	250
<b>3</b>	480	650	300	300	300	300	450	500
<b>5</b>	480	325	250	240	300	300	300	500
<b>10</b>	480	250	250	180	300	300	300	250
<b>15</b>	290	200	250	180	225	200	150	250
<b>20</b>	230	125	100	180	150	100	150	250
<b>25</b>	200	50	50	60	75	100	150	250

Table 4.6: Time (in  $s$ ) to identify simulated bias of  $1 \times 10^{-6}$

Initialization Period ( $s$ )	Window Size ( $s$ )							
	10	25	50	60	75	100	150	250
<b>3</b>	1760	2925	1750	1440	1800	1700	1350	1500
<b>5</b>	1670	1200	1250	1260	1275	1200	1200	1500
<b>10</b>	1460	875	1150	1200	1200	1100	450	500
<b>15</b>	1460	875	1100	1140	225	200	450	250
<b>20</b>	1080	875	950	780	225	200	150	250
<b>25</b>	1070	850	750	600	150	200	150	250

Table 4.7: Time (in  $s$ ) to identify simulated bias of  $5 \times 10^{-7}$

Initialization Period ( $s$ )	Window Size ( $s$ )							
	10	25	50	60	75	100	150	250
<b>3</b>	4380	4650	3700	3660	3525	2400	4500	4000
<b>5</b>	4160	4050	2600	1440	1500	1400	1800	1500
<b>10</b>	4100	3525	1750	1380	1350	1400	1350	500
<b>15</b>	3900	3375	1350	1380	1350	1300	600	500
<b>20</b>	3860	3250	1250	1260	1200	800	300	500
<b>25</b>	3260	3200	300	1200	825	400	300	250

Table 4.8: Time (in  $s$ ) to identify simulated bias of  $1 \times 10^{-7}$

Initialization Period ( $s$ )	Window Size ( $s$ )							
	10	25	50	60	75	100	150	250
<b>3</b>	Not identified	Not identified	4650	4200	4575	5400	5100	5250
<b>5</b>	Not identified	4700	4650	4020	4050	5000	4800	4500
<b>10</b>	4760	4600	4150	3960	3975	4500	4050	3250
<b>15</b>	4690	4125	4080	3960	3975	4000	3300	2000
<b>20</b>	4600	4125	3900	3900	3975	3200	2550	750
<b>25</b>	4550	4125	3900	3660	3600	2700	1800	250

The thresholds were able to flag biased data points with varying levels of effectiveness. For the larger bias slopes ( $1 \times 10^{-4}$ ,  $5 \times 10^{-5}$ , and  $1 \times 10^{-5}$ ), the biases were identified quickly (less than 500 *s*, or 8.3 *min*). For the larger bias slopes, the shorter initialization periods and smaller window sizes identified the bias faster than the larger initialization periods and larger window sizes. Typically, the larger initialization periods and window sizes were able to identify the bias in one or two cycles; however, each of those cycles was longer than the few cycles needed for the shorter initialization periods and smaller window sizes. Conversely, for the smaller bias slopes ( $1 \times 10^{-6}$ ,  $5 \times 10^{-7}$ ,  $1 \times 10^{-7}$ ), the combination of longer initialization periods and larger window sizes was faster at identifying the bias. For the bias slope of  $5 \times 10^{-6}$  all combinations of initialization period and window size were similarly effective at identifying the simulated bias.

The moving average of the residuals from Figure 4.11 identified a first-order bias with a slope of  $-2 \times 10^{-6} \frac{m/s}{s}$ . In most of the cases illustrated in Figure 4.21 and Figure 4.22, the deviation was identified. For a bias with a slope of  $-2 \times 10^{-6} \frac{m/s}{s}$ , most combinations of initialization period and window size would effectively identify the bias. The longer initialization periods and larger window sizes may slightly outperform the shorter initialization periods and smaller window sizes.

A subset of the combinations of bias slope, window size, and initialization period for satellite 31 are illustrated in Figure 4.31 and Figure 4.32. The downsampling and thresholding results for satellite 31 match those of satellite 14. Like with satellite 14, the larger bias slopes were more quickly identified by the shorter initialization periods and smaller window sizes. The smaller bias slopes were more quickly identified by the longer initialization periods and larger window sizes.

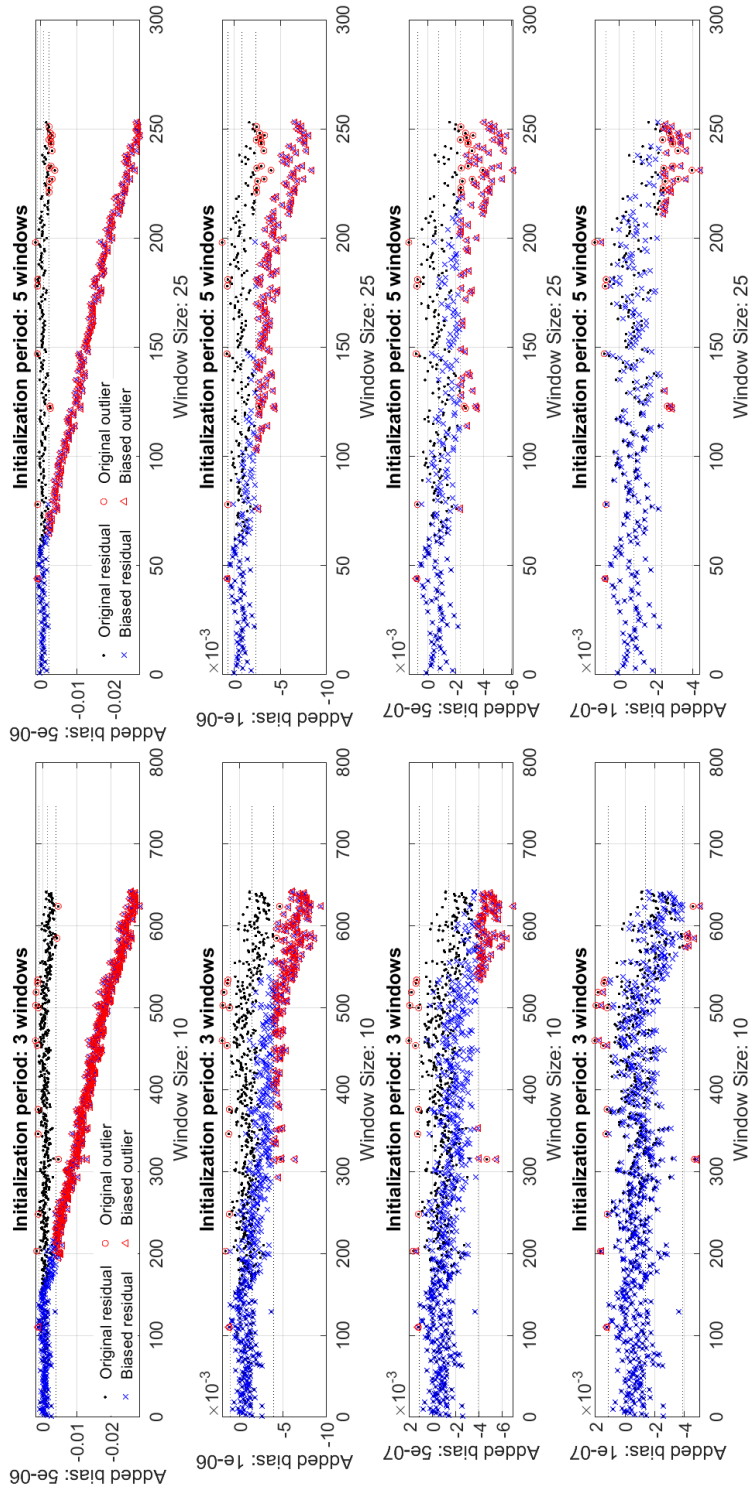


Figure 4.31: Variation of added bias, initialization period, and window size for residuals for satellite 31, Part A

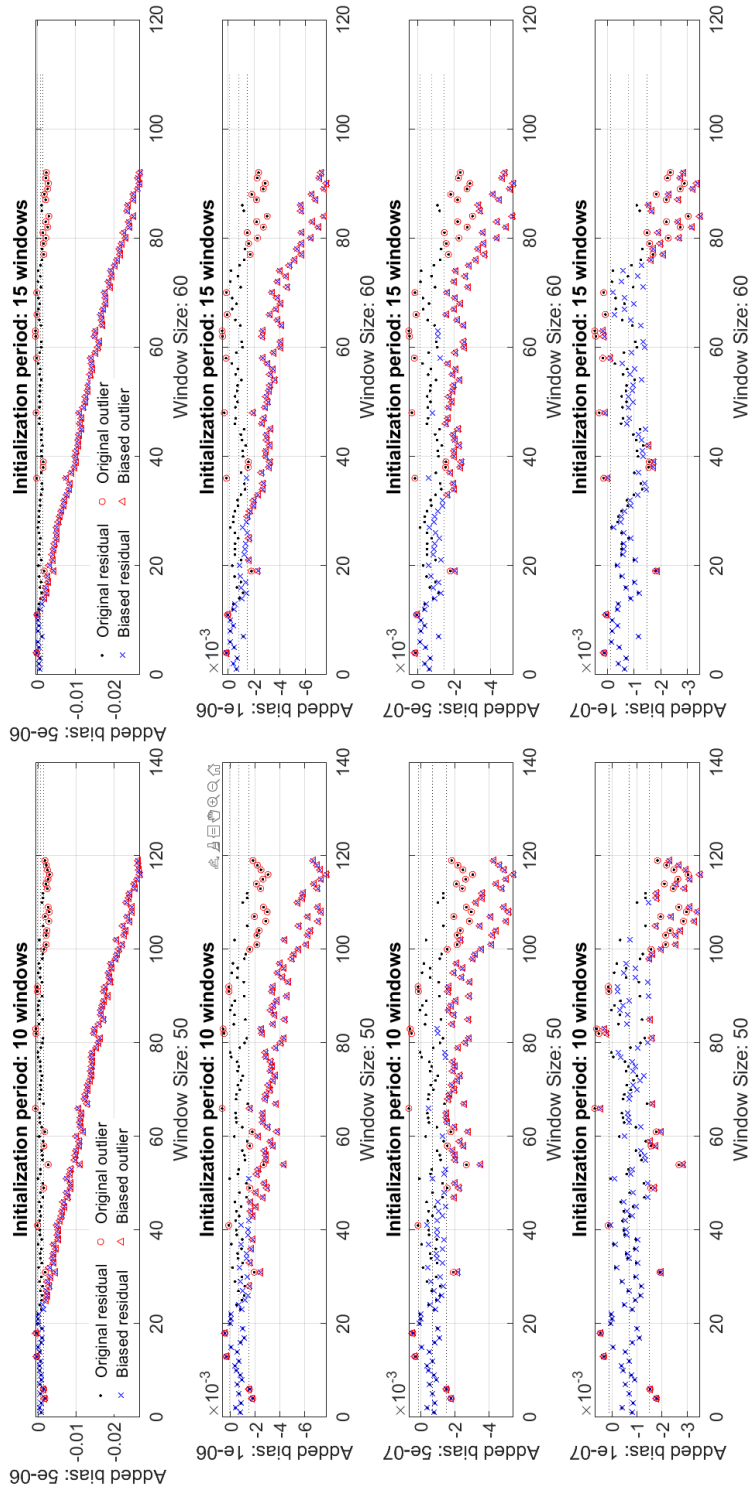


Figure 4.32: Variation of added bias, initialization period, and window size for residuals for satellite 31, Part B

# Chapter 5

## Conclusion

### 5.1 Detect and Identify Error Sources

The results and analysis for satellite 14 and satellite 31 were presented in Section 4. The results and analysis for satellite 31 matched those from satellite 14, demonstrating repeatability of the methodology. The residuals from RANSAC and TDCP were able to detect and identify a variety of error sources. The downsampling and thresholding method was able to identify zeroth-order deviations. Clusters of deviations were able to identify first-order deviations with slopes on the orders of magnitude of  $10^{-4}$  down to  $10^{-7}$  after seconds (for larger bias slopes) or hours (for smaller bias slopes). The autocorrelation and Allan variance analysis were not good indicators of initialization period and window size. Instead, a user should select combinations of initialization periods and window sizes based on the magnitude of deviations they are looking to discover. Additionally, detection should not be limited to just one solution methodology; instead, this method should be used in conjunction with other detection methods.

The multipath errors manifested as random noise. The correlated noise likely resulted from a combination of the ionospheric delays, tropospheric delays, and errors in the esti-

mation of the velocity solution. Additionally, inter-system timing biases could have lead to further deviations. The zeroth-order and larger deviations could have been caused by errors in satellite orbit prediction and multipath. The first-order deviations and smaller deviations could have been caused by ionospheric and tropospheric delays.

Autocorrelation analysis and Allan variance analysis identified other underlying properties of the data, such as an autocorrelated feature with a time constant around 1000  $s$  to 1800  $s$ . However, after residuals from low satellite angles were removed, the autocorrelation suggested the residuals were randomly distributed. The Allan variance analysis of the truncated data suggested the presence of a correlated noise process. Therefore, the assumption that the residuals were independent with time was valid.

## 5.2 Recommendations for Future Work

Once multi-GNSS navigation is feasible, the next step would be to compare it to other sources of PNT data. Different uses of PNT information have different requirements for precision, so PNT information does not necessarily have to come from a high-accuracy timing signal. Instead of a GPS signal, waves from other parts of the spectrum (*e.g.*, acoustic, ultrasonic, visible light, radio signals, magnetic waves, cell phone signals) can be used to determine location using time of arrival (TOA), angle of arrival (AOA), time difference of arrival (TDOA), or time of flight (TOF) calculations.<sup>4,12,13</sup> Pedestrian dead reckoning uses an inertial navigation unit (INU) to keep track of changes in position from a known starting point.<sup>4,13</sup> The signals from from multiple known Wi-Fi routers can use relative signal strength (RSS) to determine location.<sup>4,13,39</sup>

If the area is well mapped, then these signals of opportunity can be correlated to the map to further increase PNT confidence anywhere from 45% to 75%.<sup>37</sup> All of these indicators can be used individually or in parallel to increase the confidence in all-source navigation.<sup>18</sup>

Instead of comparing different GNSS constellations to each other, different PNT technologies can be compared to each other. See Tariq, et *al.*<sup>4</sup> for a more detailed breakdown of each of these technologies.

The operational effectiveness of implementing the multi-GNSS navigation corrections should be studied in realistic settings. While ground and flight tests in operationally relevant environments would be preferred, the use of modeling and simulation tools may be a sufficient alternative. The Air Force Research Lab's Sensors Directorate (AFRL/RY), Aerospace Systems Directorate (AFRL/RQ), or Space Vehicles Directorate (AFRL/RV) may be well-positioned to undertake such an analysis.

Lastly, the methods described here can be applied to other areas for error detection. Most time-series signals can be monitored for consistency. Other approaches rely on machine-learning algorithms to identify errors in data sets.<sup>21</sup>

# References

- [1] BA Kumar Babu. Method and system for resolving double difference GPS carrier phase integer ambiguity utilizing decentralized Kalman filters, Sep 1995. US Patent 5,451,964.
- [2] Gerhard Beutler, Jan Kouba, and Tim Springer. Combining the orbits of the IGS analysis centers. *Bulletin Géodésique*, 69(4):200–222, December 1995. doi: 10.1007/bf00806733. URL <https://doi.org/10.1007/bf00806733>.
- [3] Gerhard Beutler, Rolf Dach, Oliver Montenbruck, Urs Hugentobler, Georg Weber, and Elmar Brockmann. GLONASS and multi-GNSS in the IGS: Lessons learned from GLONASS service disruptions. In *13th Meeting of the National Space-Based Positioning, Navigation, and Timing (PNT) Advisory Board*. International Association of Geodesy, 2014. doi: 10.7892/BORIS.53907. URL <https://boris.unibe.ch/53907/>.
- [4] Zain Bin Tariq, Dost Muhammad Cheema, Muhammad Zahir Kamran, and Ijaz Haider Naqvi. Non-GPS positioning systems. *ACM Computing Surveys*, 50(4):1–34, Aug 2017. doi: 10.1145/3098207. URL <https://doi.org/10.1145/3098207>.
- [5] Andreas Brack. *Partial Carrier-Phase Integer Ambiguity Resolution for High Accuracy GNSS Positioning*. Dissertation, Technische Universität München, München, 2019.
- [6] Piet M.T. Broersen. *Automatic Autocorrelation and Spectral Analysis*. Springer London, 2006. ISBN 9781846283291.
- [7] George W Bush. U.S. space-based position, navigation, and timing policy. *National Security Policy Directive*, 39, December 2004. URL <https://fas.org/irp/offdocs/nspd/nspd-39.htm>.
- [8] Gaetano Castaldo, Antonio Angrisano, Salvatore Gaglione, and Salvatore Troisi. P-ransac: an integrity monitoring approach for GNSS signal degraded scenario. *International Journal of Navigation and Observation*, 2014, 2014.
- [9] Varun Chandola, Arindam Banerjee, and Vipin Kumar. Anomaly detection. *ACM Computing Surveys*, 41(3):1–58, July 2009. doi: 10.1145/1541880.1541882. URL <https://doi.org/10.1145/1541880.1541882>.

- [10] William J Clinton. Statement by the President regarding the United States’ decision to stop degrading global positioning system accuracy. In *Office of Science and Technology Policy*, Washington, DC, 2000. Office of the Press Secretary.
- [11] John C Cohenour. *Global positioning system clock and orbit statistics and precise point positioning*. PhD thesis, Ohio University, 2009.
- [12] Azusa Danjo, Yuki Watase, and Shinsuke Hara. A theoretical error analysis on indoor TOA localization scheme using unmanned aerial vehicles. In *IEEE 81st Vehicular Technology Conference*, pages 1–5. IEEE, 2015.
- [13] Davide Dardari, Pau Closas, and Petar M Djurić. Indoor tracking: Theory, methods, and technologies. *IEEE Transactions on Vehicular Technology*, 64(4):1263–1278, 2015.
- [14] Thomas Dautermann, Christoph Mayer, Felix Antreich, Andriy Konovaltsev, Boubeker Belabbas, and Ulrich Kalberer. Non-gaussian error modeling for gbas integrity assessment. *IEEE transactions on aerospace and electronic systems*, 48(1):693–706, 2012.
- [15] Naser El-Sheimy, Haiying Hou, and Xiaoji Niu. Analysis and modeling of inertial sensors using allan variance. *IEEE Transactions on Instrumentation and Measurement*, 57(1): 140–149, January 2008. doi: 10.1109/tim.2007.908635. URL <https://doi.org/10.1109/tim.2007.908635>.
- [16] Federal Aviation Administration. GNSS frequently asked questions, Dec 2016. URL [https://www.faa.gov/about/office\\_org/headquarters\\_offices/ato/service\\_units/techops/navservices/gnss/faq/gps/](https://www.faa.gov/about/office_org/headquarters_offices/ato/service_units/techops/navservices/gnss/faq/gps/).
- [17] Martin A Fischler and Robert C Bolles. Random sample consensus: a paradigm for model fitting with applications to image analysis and automated cartography. *Communications of the ACM*, 24(6):381–395, 1981.
- [18] Kenneth A Fisher and John F Raquet. Precision position, navigation, and timing without the global positioning system. *Air & Space Power Journal*, pages 24–33, 2011.
- [19] Thomas Friederichs. *Analysis of geodetic time series using Allan variances*. PhD thesis, Universität Stuttgart, 2010. URL <http://elib.uni-stuttgart.de/handle/11682/3866>.
- [20] JG García, PI Mercader, and Carlos H Muravchik. Use of GPS carrier phase double differences. *Latin American applied research*, 35(2):115–120, 2005.
- [21] Alexander Geiger, Dongyu Liu, Sarah Alnegheimish, Alfredo Cuesta-Infante, and Kalyan Veeramachaneni. TadGAN: Time series anomaly detection using generative adversarial networks. *arXiv preprint arXiv:2009.07769*, 2020.

- [22] Markus Goldstein and Seiichi Uchida. A comparative evaluation of unsupervised anomaly detection algorithms for multivariate data. *PLOS ONE*, 11(4), April 2016. doi: 10.1371/journal.pone.0152173. URL <https://doi.org/10.1371/journal.pone.0152173>.
- [23] GPS.gov. Timing applications, Nov 2019. URL <https://www.gps.gov/applications/timing/>.
- [24] GPS.gov. Other global navigation satellite systems (GNSS), Jan 2020. URL <https://www.gps.gov/systems/gnss/>.
- [25] R.M. Gray and D.L. Neuhoff. Quantization. *IEEE Transactions on Information Theory*, 44(6):2325–2383, 1998. doi: 10.1109/18.720541. URL <https://doi.org/10.1109/18.720541>.
- [26] Jake Griffiths and Jim R. Ray. On the precision and accuracy of IGS orbits. *Journal of Geodesy*, 83(3-4):277–287, February 2009. doi: 10.1007/s00190-008-0237-6. URL <https://doi.org/10.1007/s00190-008-0237-6>.
- [27] Steve Hilla. The extended standard product 3 orbit format (SP3-c). Technical report, National Geodetic Survey, National Oceanic and Atmospheric Administration, 2010. URL <https://files.igs.org/pub/data/format/sp3c.txt>.
- [28] David C Jefferson and Yoaz E Bar-Sever. Accuracy and consistency of broadcast GPS ephemeris data. In *Proceedings of the 13th International Technical Meeting of the Satellite Division of The Institute of Navigation (ION GPS 2000)*, pages 391–396. Institute of Navigation, 2000.
- [29] Elliott D Kaplan and Christopher J Hegarty. *Understanding GPS/GNSS: Principles and Applications*. Artech House, third edition, 2017.
- [30] Samer Khanafseh, Birendra Kujur, Mathieu Joerger, Todd Walter, Sam Pullen, Juan Blanch, Kevin Doherty, Laura Norman, Lance de Groot, and Boris Pervan. GNSS multipath error modeling for automotive applications. In *Proceedings of the 31st International Technical Meeting of The Satellite Division of the Institute of Navigation (ION GNSS 2018)*. Institute of Navigation, October 2018. doi: 10.33012/2018.16107. URL <https://doi.org/10.33012/2018.16107>.
- [31] Tomislav Kos, Ivan Markezic, and Josip Pokrajcic. Effects of multipath reception on GPS positioning performance. In *Proceedings ELMAR-2010*, pages 399–402. IEEE, 2010.
- [32] Philip Kwan. *NAVSTAR GPS Space Segment/Navigation User Segment Interfaces*, k edition, May 2019. IS-GPS-200K.
- [33] Philip Kwan. *NAVSTAR GPS Space Segment/Navigation User Segment L5 Interfaces*, f edition, May 2019. IS-GPS-705F.

- [34] Bofeng Li, Zhetao Zhang, Yunzhong Shen, and Ling Yang. A procedure for the significance testing of unmodeled errors in GNSS observations. *Journal of Geodesy*, 92(10): 1171–1186, January 2018. doi: 10.1007/s00190-018-1111-9. URL <https://doi.org/10.1007/s00190-018-1111-9>.
- [35] Jinyu Li, Li Deng, Reinhold Haeb-Umbach, and Yifan Gong. Fundamentals of speech recognition. *Robust Automatic Speech Recognition*, pages 9–40, 2016.
- [36] Yiran Luo, Jian Li, Chunyang Yu, Bing Xu, You Li, Li-Ta Hsu, and Naser El-Sheimy. Research on time-correlated errors using allan variance in a kalman filter applicable to vector-tracking-based GNSS software-defined receiver for autonomous ground vehicle navigation. *Remote Sensing*, 11(9):1026, April 2019. doi: 10.3390/rs11091026. URL <https://doi.org/10.3390/rs11091026>.
- [37] Mahdi Maaref and Zaher M Kassas. Ground vehicle navigation in GNSS-challenged environments using signals of opportunity and a closed-loop map-matching approach. *Transactions on Intelligent Transportation Systems*, 2019.
- [38] VB Mendes and RB Langley. Tropospheric zenith delay prediction accuracy for airborne gps high-precision positioning. In *Proceedings of the Institute of Navigation 54th Annual Meeting*. Institute of Navigation, June 1998. URL <https://doi.org/10.33012/2020.17163>.
- [39] Ana Moragrega, Pau Closas, and Christian Ibars. Potential game for energy-efficient RSS-based positioning in wireless sensor networks. *IEEE Journal on Selected Areas in Communications*, 33(7):1394–1406, 2015.
- [40] National Aeronautics and Space Administration. GNSS orbit products, Mar 2020. URL [https://cdis.nasa.gov/Data\\_and\\_Derived\\_Products/GNSS/orbit\\_products.html](https://cdis.nasa.gov/Data_and_Derived_Products/GNSS/orbit_products.html).
- [41] Xiaoji Niu, Qijin Chen, Quan Zhang, Hongping Zhang, Jieming Niu, Kejie Chen, Chuang Shi, and Jingnan Liu. Using Allan variance to analyze the error characteristics of GNSS positioning. *GPS solutions*, 18(2):231–242, April 2014. doi: 10.1007/s10291-013-0324-x. URL <https://doi.org/10.1007/s10291-013-0324-x>.
- [42] XJ Niu, Q Zhang, and HP Zhang. Use Allan variance to analyze the results of GNSS/INS navigation systems. In *Proceedings of the CPGPS 2010 Technical Forum on Satellite Navigation and Positioning, Shanghai, China*, pages 565–572, 2010.
- [43] United States Department of Defense. *National Defense Strategy of the United States of America*. United States Department of Defense, 2018.
- [44] United States Department of Defense. *Global Positioning System Standard Positioning Service Performance Standard*, fifth edition, April 2020.

- [45] United States Chairman of the Joint Chiefs of Staff. *National Military Strategy*. United States Chairman of the Joint Chiefs of Staff, 2018.
- [46] United States White House Office. *National Security Strategy of the United States of America*. United States White House Office, 2017.
- [47] Ahmed Radi, Sameh Nassar, Maan Khedr, Naser El-Sheimy, Roberto Molinari, and Stéphane Guerrier. Improved stochastic modelling of low-cost GNSS receivers positioning errors. In *2018 IEEE/ION Position, Location and Navigation Symposium (PLANS)*, pages 108–117. IEEE, 2018.
- [48] Benjamin W Remondi. Extending the national geodetic survey standard GPS orbit formulas. Technical Report NOS 133 NGS 46, National Oceanic and Atmospheric Administration, 1989.
- [49] Georg Schroth, Markus Rippl, Alexandru Ene, Juan Blanch, Boubeker Belabbas, Todd Walter, Per Enge, and Michael Meurer. Enhancements of the range consensus algorithm (RANCO). In *Proceedings of the ION GNSS Conference*, pages 93–103, 2008.
- [50] Nihar N. Shah, Zhen Zhu, Eric Vinande, and Jason Pontious. The feasibility of observing user-segment faults in the residuals of a consensus-based multi-GNSS solution. In *Proceedings of the 2020 International Technical Meeting of The Institute of Navigation*. Institute of Navigation, February 2020. doi: 10.33012/2020.17163. URL <https://doi.org/10.33012/2020.17163>.
- [51] *Global Navigation Satellite Systems – What’s up?*, June 2019. Space-Based Position, Navigation & Timing National Advisory Board.
- [52] J. J. Spilker. GPS signal structure and performance characteristics. *Navigation*, 25(2): 121–146, June 1978. doi: 10.1002/j.2161-4296.1978.tb01325.x. URL <https://doi.org/10.1002/j.2161-4296.1978.tb01325.x>.
- [53] Michael L. Stein. *Interpolation of Spatial Data*. Springer, 12 2012. ISBN 9781461214946.
- [54] GDAL Team. Satellite of GDAL, 2010. Licensed under CC BY-SA.
- [55] Charles Therrien and Murali Tummala. *Probability and Random Processes for Electrical and Computer Engineers*. CRC Press LLC, 09 2018. ISBN 9781439897492.
- [56] Bryan Townsend and Patrick Fenton. A practical approach to the reduction of pseudorange multipath errors in a ll gps receiver. In *Proceedings of the 7th International Technical Meeting of the Satellite Division of the Institute of Navigation, Salt Lake City, UT, USA*. Institute of Navigation, 1994.
- [57] James B Tsui. *Fundamentals of Global Positioning System Receivers: A Software Approach*. John Wiley & Sons, 2 edition, 2005.

- [58] A. Tuka and A. El-Mowafy. Performance evaluation of different troposphere delay models and mapping functions. *Measurement*, 46(2):928–937, February 2013. doi: 10.1016/j.measurement.2012.10.015. URL <https://doi.org/10.1016/j.measurement.2012.10.015>.
- [59] Frank van Graas and Andrey Soloviev. Precise velocity estimation using a stand-alone GPS receiver. *Navigation*, 51(4):283–292, 2004.
- [60] Marc Weiss, Pradipta Shome, and Ron Beard. On-board GPS clock monitoring for signal integrity. In *Proceedings of the 42nd Annual Precise Time and Time Interval Systems and Applications Meeting*, pages 465–480. National Institute of Standards and Technology, 2010.
- [61] Asmamaw Yehun, Tsegaye Kassa, Martin Vermeer, and Addisu Hunegnaw. Higher order ionospheric delay and derivation of regional total electron content over ethiopian global positioning system stations. *Advances in Space Research*, May 2020. doi: 10.1016/j.asr.2020.04.035. URL <https://doi.org/10.1016/j.asr.2020.04.035>.
- [62] W Yu, G Lachapelle, and S Skone. PLL performance for signals in the presence of thermal noise, phase noise, and ionospheric scintillation. In *Proceedings of the 19th International Technical Meeting of the Satellite Division of The Institute of Navigation (ION GNSS 2006)*, pages 1341–1357, 2006.
- [63] Eva Žáčková, Samuel Prívará, Zdeněk Váňa, and Jiří Cigler. Building modeling: on selection of the model complexity for predictive control. In *Computer Aided Chemical Engineering*, volume 32, pages 205–210. Elsevier, 2013.
- [64] Chunxi Zhang, Xianmu Li, Shuang Gao, Tie Lin, and Lu Wang. Performance analysis of global navigation satellite system signal acquisition aided by different grade inertial navigation system under highly dynamic conditions. *Sensors*, 17(5):980, April 2017. doi: 10.3390/s17050980. URL <https://doi.org/10.3390/s17050980>.
- [65] Xin Zhang, Yong Li, Peter Mumford, and Chris Rizos. Allan variance analysis on error characters of MEMS inertial sensors for an FPGA-based GPS/INS system. In *Proceedings of the International Symposium on GPS/GNSS*, pages 127–133, 2008.
- [66] Zhen Zhu, Eric Vinande, and Maarten Uijt de Haag. Multi-constellation time-differenced carrier phase solution with protection from multiple failures. In *2018 IEEE/ION Position, Location and Navigation Symposium (PLANS)*, pages 336–348. IEEE, 2018.
- [67] Zhen Zhu, Eric Vinande, Jason Pontious, and Nihar Shah. A robust multi-constellation time-differenced carrier phase solution. *GPS Solutions*, 2021. Unpublished.
- [68] C. Zucca and P. Tavella. The clock model and its relationship with the allan and related variances. *IEEE Transactions on Ultrasonics, Ferroelectrics and Frequency Control*, 52

(2):289–296, February 2005. doi: 10.1109/tuffc.2005.1406554. URL <https://doi.org/10.1109/tuffc.2005.1406554>.